Statistical Clutter Modeling and Localization and Characterization of buried Objects using Frequency Domain Electromagnetic Induction Sensing

A Thesis Presented

by

Mustafa Ozdemir

to

The Electrical and Computer Engineering Department

in Partial Fulfillment of the Requirements

for the Degree of

Master of Science

in the field of

Electrical Engineering

Northeastern University

Boston, Massachusetts

March 2001

Preface

In this thesis we address the issues related to the application of broadband electromagnetic induction (BEMI) methods to the characterization and classification of buried landmines. We consider the development of a tractable, physical model to describe an BEMI system and associated statistical signal processing algorithms to extract from BEMI data collected over a grid of points in the neighborhood of the object information regarding the location, orientation and structure of a buried object by estimating its dipole moment spectra. Algorithmically, we shall discuss two methods for extracting this information from the data. The first is an exact maximum likelohood estimator of the DMS, location, and orientation paramaters. As the ML approach is computationally intensive, we have also built a fast paramater extraction technqiue whose performance is quite comprable to that of the ML estimator.

In the case of low metal content mines where the SNR can be a problem, we also have developed and verified new clutter mitigation techniques. Current clutter

processing basically amounts to background subtraction; i.e. data collected in a region near the mine is averaged and subtracted from data taken over the mine. This approach ignores much of the spatial correlation in the background clutter and all correlation from frequency to frequency. Thus, here we develop a more complete stochastic model and assoiated estimation/subtraction processing methods which takes into account these correlation effects.

We verify the peformance of our models and algorithms using both simulated data and real sensor data collected with the GEM-3 instrument for high metal and low metal content mines.

Contents

List of Figures

List of Tables

Chapter 1

Introduction

Electromagnetic induction (EMI) systems represent one of the more common sensing technologies for the detection and localization of buried metallic objects including landmines and unexploded ordinance(UXO). While many system, such as the EM61, operate essentially in the time domain using pulsed induction principals, there has been significant interest recently in the use of swept frequency measurement systems to perform so-called broadband electromagnetic induction (BEMI). Indeed, work in [1] indicates that data taken over a band from tens of Hertz to tens of kHz convey information not only about presence of absence of an object but can also be used to determine object shape, size, orientation, and material characteristics; i.e. to perform object characterization.

1.1 Background

In the last years, considerable effort has been dedicated to the processing of both time and frequency domain EMI data. Most of the work has paid attention to the problem of object detection (is there anything over there?) with some developments on the problems of discrimination and classification (If there is, how is it like?). Most methods make use of a physical model for the scattering of low frequency electromagnetic fields from UXO-type objects within a statistical signal processing context. These statistical methods offer a solid theoretical and algorithmic basis for the use of estimation procedures to decide parameters in the physical models and hypothesis testing methods to detect and discriminate the object. A concise overview of the work most relevant to that being presented here is given in the following paragraphs.

In the area of frequency domain EMI, significant new work has been devoted to the electromagnetic induction spectroscopy (EMI) technique [16, 18, 20]. The fundamental idea for EMI is to gather a vector of frequency domain EMI samples directly over a target. Discrimination is achieved by comparing that vector to a library of previously obtained sample waveforms and selecting the library element providing the closest equivalent. The method is encouraged by the experimental observation that clutter objects have markedly different spectra from UXO. As this process is rather robust to uncertainly in object burial depth [18], no work has been given an account on robustness of EMI to errors in sensor location over the target.

In the same way, little effort has been spent to the use of BEMI for processing data collected at multiple points in space. Lastly, the BEMI solution recommended to the unknown orientation problem has been to gather data using orthogonal orientations of the sensor over the target as a means of synthesizing data from an random orientation. While experimental results of synthesis have been given for a 37mm projectile [16], the wider validity of this method and its applicability to discrimination are far from obvious both in the theory and in practice.

In [15], the authors show an exact EMI scattering model founded on a body of revolution integral equation solution to Maxwell's equations. Their work gives a theoretical base for the utility of a frequency response model as a superposition of single pole transfer functions or decaying exponentials in the time domain. Before using these poles as features for separating clutter from UXO, the pole-based discrimination methods of [13] compare experimental spectral data against spectra constructed using these pole-only models; that is like BEMI, discrimination is done in the data domain rather that in feature space. While in principle these poles should be independent to orientation, the representative poles used to characterize a particular object were obtained experimentally by averaging the estimates from data taken with the object at three orientations. Similarly, the position and orientation dependence of the expansion coefficients for each 1-pole portion of the model was dealt with a rather ad hoc manner by normalizing the data. The precise scattering model of [15]

has also been used to generate target signatures for the detection methods of [13]. There a Bayesian statistical framework was used to average out uncertainties in object position. In [14] Gao et al. took into account other detection methods which could process either the full frequency domain signature at one point over target(like BEMI) or the energy in the signal from multiple points; on the other hand no methods for processing the full set of data collected over all of space have been given details from this group.

1.2 Contributions

In this section, I review the contributions of this thesis to the solution of two problems related to the application of BEMI systems to the characterization and classification of buried objects. The first problem considered in this thesis is that for high metal content (HMC) objects, the signal arising from the object under investigation is larger enough than the signal arising from volumetric inhomogeneties in the electromagnetic properties of the earth (permitivity and conductivity). Therefore, I assume that this signal contains data and noise. However, for the second problem involving low metal content (LMC) objects, the signal from the earth can be of the same order or magnitude as much as the signal from the object so this "clutter data" is entered the signal data additively besides the data and noise.

In this thesis, I consider the development of a tractable, physical model to describe

an BEMI system and associated processing methods to extract from BEMI data information regarding the location, orientation and structure of a buried object. Assuming that the incident EMI field is uniform over the support of the object, the model approximates the scattering properties of the object in terms of dipole-pole moment spectra (DMS) which can be used to easily determine the fields observed by the EMI receiver. From an inversion perspective, the idea underlying the work in this thesis is that successful estimation of these moment spectra can form the basis for object classification and identification. Also, it is noted that, unlike general finite element, boundary element, or finite difference type scattering models, the one considered here is particularly well suited for the processing tasks at hand because it is parameterized directly in terms of the quantities of interest: the DMS, the co-ordinates of the object center, and the three rotation angles used to define the orientation of the scatterer relative to a global, Cartesian frame.

In the following chapters, I have presented two approaches. The first approach for the first problem is for the estimation of the dipole moment spectra (DMS), the co-ordinates of the object center, and the rotation angles from EMIS data for HMC objects. Under this approach, the data are linearly related to the dipole moment spectra and non-linear functions of the object location and rotation angles. I determined the object center and rotation angles by using a low-dimensional non-linear optimization method and employed a linear least square inversion procedure to determine the

estimates of DMS.

The second approach is for the estimation of the DMS, the co-ordinates of the object center, and rotation angles from BEMI data after removing the estimation of clutter from the signal for the case of LMC objects. Under this approach, I first estimated the distribution of clutter by using a stochastic model. Then, I determined the parameters of the target after cleaning the signal.

In the second approach, it is proposed to model the clutter as a correlated random field which can be described using a polynomial regression model the structure of which is motivated by examination of real clutter data collected with a GEM-3 [3, 5] sensor. The estimate then subtract processing strategy I propose is designed to reflect the way in which BEMI-type sensors are employed in the field. Currently clutter mitigation amounts to subtracting from data taken in the immediate vicinity of the object target-free secondary data taken on the boundary of this area. Thus, the correlation structure of the clutter is not properly accounted for in the mitigation procedure. Moreover, this approach completely ignores the fact that the sensor is often calibrated in a region close to a suspected target. Thus any information which the calibration data may be able to yield regarding the clutter structure over the object is also absent from the processing.

Here I consider a model-based approach to BEMI clutter mitigation. The data from the calibration region as well as the boundary of the object region are all used

to estimate and remove the clutter in the data containing object signal.

1.3 Thesis Organization

The rest of the thesis is organized as follows. Chapter 2 contains problem formulation and physical model used. In chapter 3, I introduce the processing methods . In chapter 4, simulated and real data results will be given. Finally, in chapter 5, I summarize the results and contributions of this thesis, and indicate future research directions.

Chapter 2

Problem Formulation and Physical Model Used

In this thesis, a physical model is considered to describe a BEMI system and associated processing methods to extract the location, orientation and structure of a buried object from the BEMI data . In the first section, I describe a generalized form of an BEMI forward model based on the work of Das *et. al* [2].

Given this sensor model, I consider two problems. The first problem is the characterization and localization of the high metal content(HMC) mines. I examine estimation-theoretic methods for determinng an object's center, its orientation, and scattering characteristics (as defined by a spectrum of low order multipole moments)

from low frequency spectroscopic data obtained over a grid of spatial locations. Under this model, the data are the linear function of the dipole moment spectra and the non-linear function of the object location and rotation angles. An efficient estimation procedure based on a low-dimensional non-linear optimization routine for the determination of the object center and rotation angles is employed with the linear least squares inversion procedure which determines the estimate of the dipole moment spectra.

The second problem is low metal content(LMC) mine characterization from BEMI data. For HMC, we can ignore the interface and assume additive white sensor noise model. However, for LMC, new processing techniques are needed. In particular, for these cases the signal arising from the interface and volumetric inhomogeneities in the electromagnetic properties of the earth (permittivity and conductivity) can be of the same order or magnitude if not larger than the signal arising from the object under investigation. Moreover, this "clutter signal" is known to enter the data *additively* suggesting one method of mitigating the clutter would be to estimate and subtract it from the data.

I propose to model the clutter as a correlated random field which can be described using a polynomial regression model the structure of which is motivated by examination of real clutter data collected with a GEM-3 [3, 5] sensor. The estimate then subtract processing strategy I propose is designed to reflect the way in which

BEMI-type sensors are employed in the field.

Here I consider a model-based approach to BEMI clutter mitigation. As shown in Fig. 2.4, there is the calibration data and the data taken on the boundary of the object region. The latter one is used to estimate the clutter signal on the interior of the object region. Here I assume that the boundary data doesn't contain any mine signal. Second assumption is that there is some correlation between one region and another region in the clutter data. In the processing method the data from the calibration region as well as the boundary of the object region are all used to estimate and remove the clutter in the data containing object signal. After cleaning the data in this manner, I describe a new set of methods for estimating the object characteristics: location, orientation, and DMS.

2.1 Physical Model

In this thesis I consider an extension of a physical model for EMI proposed in [2] describing the scattering of low frequency electromagnetic radiation by spherical or spheroidal objects of known conductivity and permeability. As seen in Fig. 1 the transmitters and receivers are taken to be square coils (not necessarily co-located) with sides of length $2A$. The target center is located at $r_0 = (x_0, y_0, z_0)$ in the $x - y - z$ coordinate system. For the problems of interest in this work the effects of the low conductivity ground typically can be ignored [2] so that the entire sensor

system is taken to reside in free space.

The physical model is based on the assumption that scattering characteristics of the object of interest can be approximated using a low order dipole model. The electromagnetic force EMF, s, induced in a single turn receive coil located at r_{rec} by an object at r_0 is given as the scalar product:

$$s = \frac{i\omega\mu_o}{I} g^T M \tag{2.1}$$

where g is a 3×1 vector holding the x, y, and z components of the magnetic field produced at r_0 by a current I flowing in the receive coil, g^T indicates the transpose of g, ω is the operating frequency, $i = \sqrt{-1}$, and μ_0 is the permeability of free space. As described in Appendix A of [2], the vector g is a function only of $r_{rec} - r_0$, the relative position of the object and the sensor.

The tensor, M, defines the dipole scattering characteristics of the object. To determine the structure of M, I note that the magnetic field generated by a transmitting coil will cause a magnetizable target to polarize in such as way as to weaken the field in its interior. The precise structure of the magnetic moment induced in the object depends on its electromagnetic and geometrical parameters and the induced magnetic field of the transmit coil at r_0 in the following way

$$M = \beta_0 \Lambda f \tag{2.2}$$

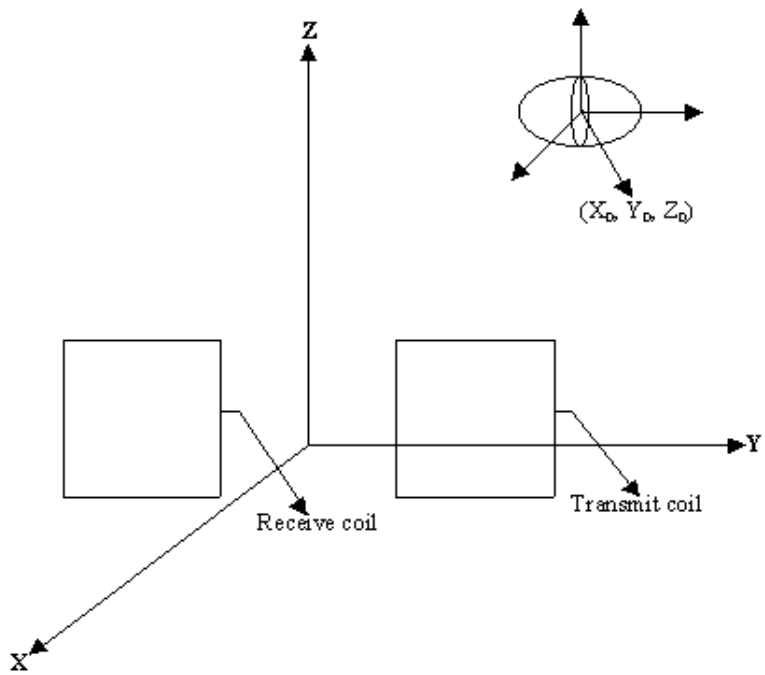

Figure 2.1: One sensor comprising sensor coils and target object.

where Λ is the normalized polarizability tensor, f is the excitation field vector evaluated at the dipole position and has a similar functional form to that of g, and $\beta_0 = 3\frac{\mu_r - 1}{\mu_r + 2}$ is the sensitivity factor for a sphere.

In this work I consider targets to be well modeled as ellipsoids. In the event that the target's axes are parallel to those of a global Cartesian co-ordinate system Λ can be represented by the matrix as follows:

$$\Lambda = \begin{bmatrix} \lambda_1(\omega) & & \\ & \lambda_2(\omega) & \\ & & \lambda_3(\omega) \end{bmatrix}. \tag{2.3}$$

The three frequency dependent λ's (here referred to as moment spectra) each are

associated with one of the principal axes of the ellipsoid. For a sphere, all three are identical and closed form expressions can be found for all orders of dipoles [1]. In [2], scattering from spheroids was considered. In such cases, two of the λ's are the same, and closed form expressions for their dipole moment structure can only be found in the case of $\omega = 0$. More recently, the work in [15] indicates how one might employ multiple poles in the complex frequency plane to accurately model the scattering process for arbitrary objects. Generally, the problem of determining the moment spectra given the axis lengths and material of the object is an open problem and one which we are currently pursuing. Here I assume that such a correspondence can be found and concentrate instead on the estimation of Λ from a given set of data.

In the event that the ellipsoid is rotated relative to the global co-ordinate system, it is necessary to mathematically express the components of g and f in the frame of the ellipsoid as follows. A Cartesian co-ordinate system $x - y - z$ is attached to the ellipsoid. I have both field vectors g and f line in the same coordinate system. A second system $x^{'''} - y^{'''} - z^{'''}$, whose axes coincide with the ellipsoid axes can be found by doing the following rotations. It is first rotated through the angle of ϕ about the z-axis. I obtain the new system $x^{'} - y^{'} - z^{'}$. Next the new system is rotated about $y^{'}$-axis through the angle of θ, resulting other system $x^{''} - y^{''} - z^{''}$. To complete transformation, the axes are rotated about $x^{''}$ through the angle of ψ, and I find the last system $x^{'''} - y^{'''} - z^{'''}$, coinciding with the ellipsoid axes. All rotations are shown

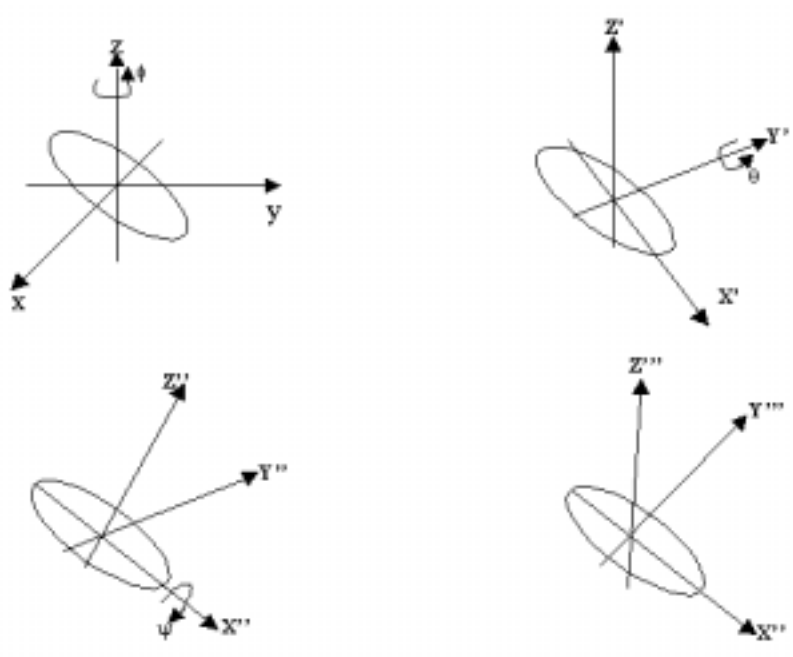

Figure 2.2: Angle transformations about three coordinate axes.

in Fig. 2. This sequence of transformations is described by the rotation matrix,

$$R = \begin{bmatrix} \cos\theta\cos\phi & \cos\theta\sin\phi & -\sin\theta \\ -\cos\psi\sin\phi + \sin\phi\sin\theta\cos\phi & \cos\psi\cos\phi + \sin\phi\sin\theta\sin\phi & \sin\phi\cos\theta \\ \sin\psi\sin\phi + \cos\psi\sin\theta\cos\phi & -\sin\psi\cos\phi + \cos\phi\sin\theta\sin\phi & \cos\phi\cos\theta \end{bmatrix} \tag{2.4}$$

The matrix R is incorporated into the model as follows

$$s = \frac{i\omega\mu_0\beta_0}{I} g^T R^T \Lambda R f \tag{2.5}$$

where the vector Rf represents the components of the transmitted fields in the coordinates of the rotated ellipsoid with an analogous interpretation for Rg.

In this work, I are concerned with processing methods based on multi-frequency data from obtained from multiple transmitter/receiver locations. Assuming I collect M frequency samples from each of N combinations of transmitters and receivers positions then I can write the kth frequency sample at the nth position as

$$s_{n,k} = \frac{i\omega_k \mu_0 \beta_0}{I} {g_n}^T R^T \Lambda_k R f_n + w_{n,k} \tag{2.6}$$

where $w_{n,k}$ is measurement noise. From this data set, our processing objectives are the estimation of clutter parameters for low metal content metal case and mine parameters for all cases and finally classification of objects. In the next section, I describe the clutter model.

2.2 Clutter model

For low metal content objects a simple additive white Gaussian noise model is not satisfactory. The interaction of the transmitted signal with the background medium, usually negligible for sensing metal objects, become prominent here. These effects are manifest in the form of additive, correlated noise in the signal which I term "clutter". In this work I develop a stochastic model describing the distribution of clutter which provides for the spatial correlation seen in this portion of the sensor signal.

As shown in Fig. 2.3 the simulated clutter data makes use of the stochastic model I will develop in the following paragraphs.

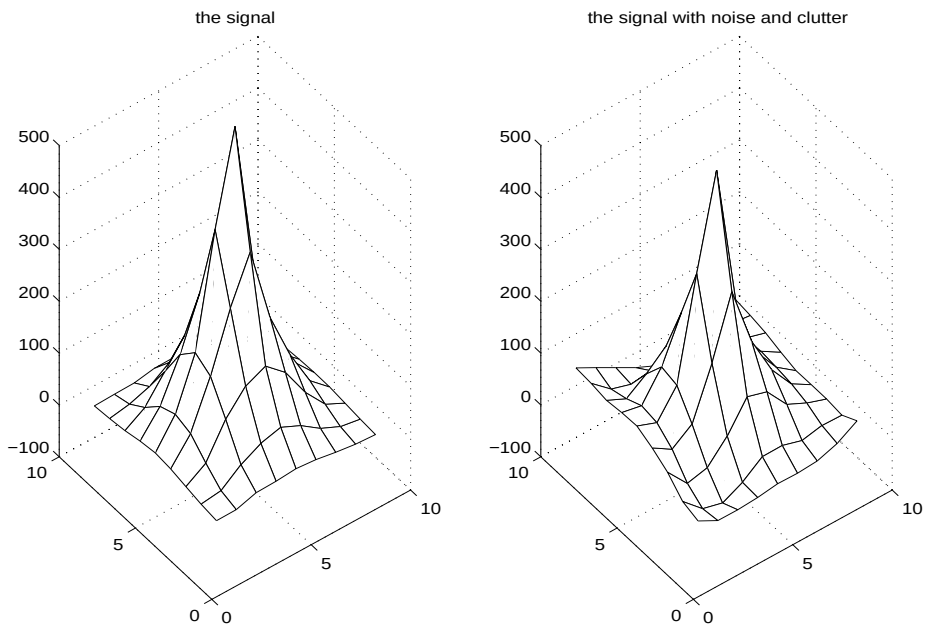

Figure 2.3: Simulated Clutter Data.

Specifically, I consider the following polynomial regression model in the spatial variables x_i and y_i, the x and y position of the ith sensor to describe this clutter at frequency ω_k:

$$c(x_i, y_i, \omega_k) = \sum_{p,q} \alpha_{p,q,k} x_i^p y_i^q + n_{i,k} \tag{2.7}$$

where the α's are unknown, random expansion coefficients, and $n_{i,k}$ represents residual, "white" variations not captured by the regression. Collecting the clutter samples

at all locations and all frequencies into a signal vector I write the overall model as

$$c = X\alpha + n. \tag{2.8}$$

For M frequencies $X = I_M \otimes X'$ where I_N is the $N \times N$ identity matrix, $\otimes$ denotes the Kronecker product and X is the block diagonal matrix obtained from all the X''s, where the element of X' for (i, j)th position is $x_i^p y_j^q$, α is the vector containing $\alpha_{p,q,k}$, and n is the noise vector.

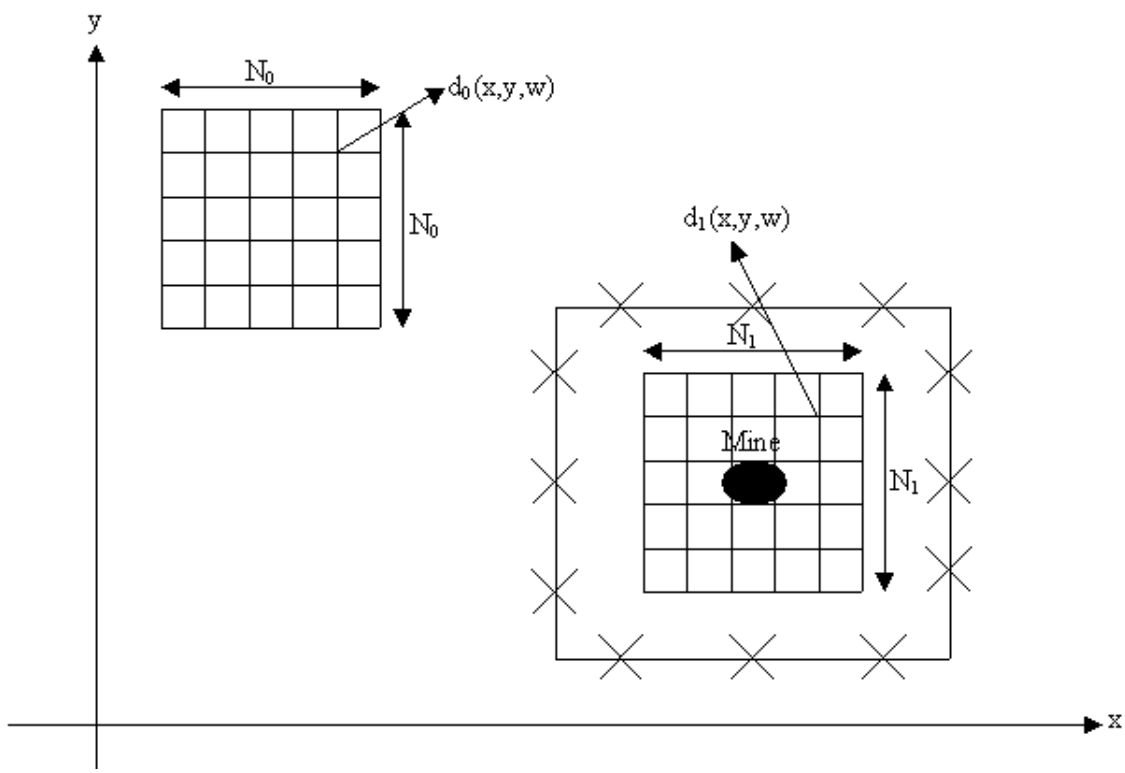

Figure 2.4: Clutter Model.

I use (2.8) to describe the distribution of clutter over two regions of space: a calibration area and a region containing an object to be characterized. As illustrated

in Fig. 2.4 the clutter mitigation procedure I propose makes use of *all* the calibration data and the data taken on the *boundary* of the object region to estimate the clutter signal on the interior of the object region. One supposition here is that the boundary data do not contain any mine signal. Another is that there is some correlation in the clutter from one region to the next which can and should be exploited in the processing. Thus, I introduce a simple statistical model linking the α vector from the clutter region to that of the object region. Formally, over the calibration region I write the clutter as

$$c_0 = X_0\alpha_0 + n_0 \tag{2.9}$$

while over the object area I have

$$c_1 = X_1\alpha_1 + n_1 = \begin{bmatrix} X_{1,b} \\ X_{1,i} \end{bmatrix} \alpha_1 + \begin{bmatrix} n_{1,b} \\ n_{1,i} \end{bmatrix}. \tag{2.10}$$

with $X_{1,i}$ built from points interior to the mine region, $X_{1,b}$ from the boundary points (marked by "X" in Fig. 2.4), $n_{1,i}$ interior noise samples and $n_{1,b}$ boundary noise samples. To complete the model of the clutter I assume that the vector α_1 is $\sim N(0, \sigma_\alpha^2 I)$, and I hypothesize that α_0 and α_1 are related via random walk type model of the form

$$\alpha_0 = \alpha_1 + n_2 \tag{2.11}$$

Finally, for simplicity I take $n_j \sim N(0, \sigma_j^2 I)$ for $j = 0, 1, 2$ in 2.9– 2.11.

In the light of these models, I describe the details of estimation processing methods in the following chapter.

Chapter 3

Processing

In this chapter, I first show how to estimate the parameters of the clutter and mitigate it. Finally, I describe the target parameter estimation algorithms.

In the previous chapter the clutter model was developed as a correlated random field which can be described using a polynomial regression model. Unlike currently clutter mitigation methods that usually amounts to subtracting from data taken in the immediate vicinity of the object target-free secondary data taken on the boundary of this area, here I consider a model-based approach to BEMI clutter mitigation in which the data from the calibration region as well as the boundary of the object region are all used to estimate and remove the clutter in the data containing object signal.

The first target parameter estimation algorithm, algorithm-I is the "optimal"

statistical algorithm and is designed for extracting the information; the DMS, the coordinates of the object center, and the three rotation angles of the object from BEMI data. Under this model, the data are linearly related to the multipole moment spectra and non-linear functions of the object location and rotation angles. This function form is exploited in the construction of an efficient estimation procedure based on a low-dimensional non-linear optimization routine required for the determination of the object center and rotation angles (6 variables in all). Embedded within this routine is an associated regularized, linear least squares inversion procedure which implicitly determines the estimates of the MMS.

Relative to the statistically optimal algorithm-I, the other one, algorithm-II is theoretically suboptimal but faster and still highly accurate.

3.1 Clutter estimation and mitigation

Given the clutter model described in the previous section, our first objective is to find an estimate of α_1 given c_0, and c_1, so that I can estimate the clutter data for the whole mine present region. Toward this end, I substitute (3.13) into (3.11) to obtain;

$$c_0 = X_0\alpha_1 + X_0 n_2 + n_0 \tag{3.1}$$

Combining this with (3.12), yields the complete clutter model

$$\underbrace{\begin{bmatrix} c_0 \\ c_1 \end{bmatrix}}_{c} = \underbrace{\begin{bmatrix} X_0 \\ X_1 \end{bmatrix}}_{D} \alpha_1 + \underbrace{\begin{bmatrix} I & 0 & X_0 \\ 0 & I & 0 \end{bmatrix}}_{E} \underbrace{\begin{bmatrix} n_0 \\ n_1 \\ n_2 \end{bmatrix}}_{n} \tag{3.2}$$

with $En \sim N(0, K)$ and $K = E \text{ blockdiag}(\sigma_0^2 I, \sigma_1^2 I, \sigma_2^2 I) \; E^T$. Eq. (3.2) provides a linear model relating all of the clutter data of interest to the expansion coefficients over the region containing the object. Using this model, the linear least squares estimate of α_1 based on the clutter data taken over the calibration region and the boundary of the mine region is [5]

$$\hat{\alpha}_1 = (D_r^T K_r^{-1} D_r)^{-1} D_r^T K_r^{-1} M_0 c \tag{3.3}$$

where M_0 is a selection matrix that extracts from c the c_0 and $c_{1,b}$ subvectors, $D_r = M_0 D$, and $K_r = M_0 K M_0^T$. Then, the estimate of the clutter data for the interior of the mine present region is

$$\hat{c} = X_{1,i}\hat{\alpha}_1 = X_{1,i}(D_r^T K_r^{-1} D_r)^{-1} D_r^T K_r^{-1} M_0 c \equiv M_1 c. \tag{3.4}$$

I mitigate the clutter in the signal as follows: Collecting the data over all frequencies and positions I write the model in (2.6) as;

$$s = s_0 + c_{1,i} + \omega = s_0 + M_2 c + \omega \tag{3.5}$$

with s_0 the vectorized form of the first term in (2.6), $c_{1,i}$ clutter on the *interior* of the object region, n noise and M_2 the matrix which extracts from c the $c_{1,i}$ subvector. The noise vector ω is $N(0, \sigma_\omega^2 I)$. Then, subtracting $\hat{c}$ from the data vector s yields the clutter mitigated data, or cleaned data, $\bar{s}$,

$$\bar{s} = s_0 + M_2 c - \hat{c} + \omega \quad = \quad s_0 + (M_2 - M_1)c + \omega \equiv s_0 + Mc + \omega$$

Thus, the cleaned data are $N(s_0, K_{\bar{s}})$ with (after some algebra)

$$\begin{aligned} K_{\bar{s}} &= M K_c M^T + \sigma_\omega^2 I \\ K_c &= \sigma_\alpha^2 D^T D + K \end{aligned}$$

3.2 Target parameter estimation

3.2.1 Algorithm-I

The model developed in the previous chapter is particularly well suited to the processing task at hand. First, the position of the target appears only in the vectors g and f and the orientation angles are seen in the matrix R. While the data are non-linear functions of these variables (six in all) the analytical nature of the model makes determination of these quantities relatively straightforward using a non-linear optimization routine. More importantly, the shape and electrical characteristics of the object are encoded in the moment spectra λ_i which are linearly related to the

data. Thus, determination of these large vectors (three complex valued unknowns per frequency) reduces to a linear least squares problem the solution of which can be obtained in closed form. In the following section, I provide a more detailed description of how these observations are exploited in the design of an efficient processing scheme.

First of all, I manipulate the model to a form that is more suitable for processing. Because $\lambda_k(\omega)$ is a complex quantity in general, so is $s_{n,k}$. Thus, after cleaning the data and separating it into real and imaginary parts, I make explicit the linear dependence of the data on the dipole moments as follows

$$\begin{bmatrix} \bar{s}^R_{n,k} \\ \\ \bar{s}^I_{n,k} \end{bmatrix} = \underbrace{\begin{bmatrix} a^R_n & 0 \\ \\ 0 & a^I_n \end{bmatrix}}_{A_n} \lambda_k + \begin{bmatrix} w^R_{n,k} \\ \\ w^I_{n,k} \end{bmatrix} \tag{3.6}$$

$$\lambda_k = [\lambda^R_{1,k}\ \lambda^R_{2,k}\ \lambda^R_{3,k}\ \lambda^I_{1,k}\ \lambda^I_{2,k}\ \lambda^I_{3,k}]^T \tag{3.7}$$

where superscript R indicates real part and superscript I indicates imaginary part. The a^R_n and a^I_n are 3×1 vectors depending on (a) r_0, (b) the locations of the transmitter and receiver, and (c) the rotation angles, $\alpha = [\theta\ \psi\ \phi]$. These vectors can be obtained from f_i, R, g_j after some straightforward algebra. Finally, the vector λ_k hold the real and imaginary parts of the samples of the three dipole moment spectra for the ellipsoid at frequency ω_k.

Stacking the data from all transmitter-receiver pairs for all frequencies gives the

discretized data model:

$$\bar{s} = A(r_o, \alpha)\lambda + w. \tag{3.8}$$

For M frequencies $A = I_M \otimes A_1$ where I_N is the $N \times N$ identity matrix, $\otimes$ denotes the Kronecker product and A_1 is the block diagonal matrix obtained from all the A_n's. Note that for if we collect data from a total of N transmitter/receiver pairs then A_i is a $2N$ by 6 matrix and A is $2NM \times 6M$. Finally, the noise vector, w, to be zero mean and Gaussian random variables with variance $K_{\bar{s}}$.

Eq. (3.8) is used in a penalized least squares approach to determine the location of the object, r_0, the orientation angles, α and dipole moments, λ. Estimates of these quantities, denoted as $\hat{r}_0$, $\hat{\alpha}$, and $\hat{\lambda}$ respectively, are defined as those values which minimize the following cost function:

$$C(r_0, \alpha, \lambda) = \|s - A(r_0, \lambda)\lambda\|^2_{K_{\bar{s}}} + \sum_{i=1}^{3} \beta_i \|L_i \lambda\|_2^2. \tag{3.9}$$

In (3.9), $K_{\bar{s}}$ is the noise covariance matrix, $\|x\|_A \equiv x^T A x$, and the L_i are used to regularize the problem by enforcing smoothness in the spectra of the dipole moment estimates. Specifically, L_i is built such that

$$\|L_i \lambda\|_2^2 = \sum_{m \in \{R,I\}} \sum_{k=1}^{M} (\lambda_{i,k}^m - \lambda_{i,k}^m)^2. \tag{3.10}$$

The regularization parameters β_i in (3.9) are used to determine the tradeoff in the reconstruction between the two terms in the cost function. The first terms enforces fidelity to the data while the second ensures smooth spectra. By providing for up

to three such parameters, I allow for flexibility in adapting the processing structure to the problem at hand. For example, in the case that we knew we were looking for spherical objects then all three λ_i function would be the same and we would require only one β. For spheroidal objects, where two of the axes are the same, only two β_i and λ_i are required: one for the major and one for the minor axis. Finally, I note that in general, the on-line determination of β_i is a well-studied, non-trivial issue beyond the scope of this thesis [6, 7, 8]. For simplicity, in the examples in Chapter 5, I assume that β is known.

To minimize the cost function, I note first that because (3.9) is quadratic with respect to λ, $\hat{\lambda}$ can be explicitly stated in terms of α and r_0 via

$$\hat{\lambda} = \left(A^T K_{\bar{s}}^{-1} A + \sum_{i=1}^{3} \beta_i L_i^T L_i \right)^{-1} A^T K_{\bar{s}}^{-1} y \equiv Q(r_0, \alpha) y \tag{3.11}$$

so that I can write:

$$\hat{r}_0, \hat{\alpha} = \arg\min_{r_0, \alpha} C(r_0, \alpha, Q(r_0, \alpha) y) \tag{3.12}$$

$$\hat{\lambda} = Q(\hat{r}_0, \hat{\alpha}) y \tag{3.13}$$

In our experiments I have found that C is generally quite well behaved with respect to the the location parameters but exhibits many local minima in terms of the orientation angles. Thus, I have adopted the following strategy for first determining rough estimates of r_0 and α and then refining these quantities. I begin by imposing a coarse grid first on the three dimensional space of all permitted orientation angles. For each

α-value in the grid, a 3D non-linear least squares solver is used to find the optimal r_0. I use that α values with the smallest overall cost and the associated estimate of r_0 for that cell to initialize a full 6D non-linear least squares scheme to find the final values of $\hat{\alpha}$ and $\hat{r}_0$. Using these values, I construct $\hat{\lambda}$ according to (3.13).

3.2.2 Algorithm-II

Given $\bar{s}$, our aim is to estimate the parameters of the detected object: the co-ordinates of the object center, the moment spectra, and the three rotation angles. Here I take a two-step approach to this procedure. First, I use the data to estimate the three location parameters of the object, (x_0, y_0, z_0) and a collection of quantities related to the Euler angles and the DMS. Second, I use these estimates to separately extract orientation and DMS information. The motivation for this approach is primarily computational. As described in greater detail below, each stage requires the solution of a problem involving a single large parameter vector which is *linearly* related to the data and a substantially smaller set of parameters for which the relationship is *non-linear*. By pursing a two step strategy, I can exploit this structure to obtain an estimation approach requiring two small non-linear search routines rather than one larger one. Moreover, the first such routine for the location parameters is better behaved in terms of local minima than the second search for the Euler angles. Thus, I are able to effectively partition the overall estimation problem.

Our approach to the first subproblem is to starts by defining the symmetric matrix M_k

$$M_k = R^T \Lambda_k R = \begin{bmatrix} \mu_{11,k} & \mu_{12,k} & \mu_{13,k} \\ \mu_{12,k} & \mu_{22,k} & \mu_{23,k} \\ \mu_{13,k} & \mu_{23,k} & \mu_{33,k} \end{bmatrix} \tag{3.14}$$

Substituting (3.15) into (2.1), "stacking" the data from all transmitter-receiver pairs for all frequencies, I arrive at the following model for the cleaned data

$$\bar{s} = B(r_0)\mu(\alpha, \lambda) + \Omega. \tag{3.15}$$

where, for M frequencies $B = I_M \otimes B_1$ with B_1 a matrix constructed from the f_n and g_n vectors. The vector μ is comprised of the six *unique* elements of each M_k. Finally, the noise vector Ω is zero mean and Gaussian with variance $K_{\bar{s}}$.

Eq. (3.15) is used in a penalized least squares approach to determine the location of the object, r_0 and μ , as follows:

$$\hat{\mu}_0, \hat{r}_0 = \arg\min_{\mu, r_0} \|\bar{s} - B(r_0)\mu\|^2_{K_{\bar{s}}} \tag{3.16}$$

The solutions [3, 5] are found:

$$\hat{r}_0 = \arg\min_{r_0} \|\bar{s} - B(r_0)(B^T(r_0)K_{\bar{s}}^{-1}B(r_0))^{-1}B^T(r_0)K_{\bar{s}}^{-1}\bar{s}\|_2^2 \tag{3.17}$$

$$\hat{\mu} = (B^T(\hat{r}_0)K_{\bar{s}}^{-1}B(\hat{r}_0))^{-1}B^T(\hat{r}_0)K_{\bar{s}}^{-1}\bar{s} \tag{3.18}$$

The goal of the second processing step is to use $\hat{\mu}$ to estimate λ and α=the vector of three Euler angles. Via (3.14), I start by using $\hat{\mu}$ to build $\hat{M}_k$ in the obvious

manner. According to (3.14), I should be able to find a *single* rotation matrix which simultaneously diagonalized *all* of the M_k's to produce the diagonal Λ_k's. I use this observation to construct the following penalized least squares cost function

$$C(\alpha_k, \lambda) = \sum_k \parallel R^T(\alpha)\hat{M}_k R(\alpha) - \Lambda'_k \parallel_F + \text{penalty} \tag{3.19}$$

where $\|X\|_F$ is the Frobenius norm of the matrix X,

$$\Lambda'_k = \begin{bmatrix} \lambda'_{11,k} & \lambda'_{12,k} & \lambda'_{13,k} \\ \lambda'_{12,k} & \lambda'_{22,k} & \lambda'_{23,k} \\ \lambda'_{13,k} & \lambda'_{23,k} & \lambda'_{33,k} \end{bmatrix}$$

is the matrix containing the moment spectra and it is not generally diagonal due to the fact that the noise in the data will prevent the exact simultaneous diagonalization of all the M_k. With this in mind, the goal of penalty is to (a) discourage nonzero off diagonal entries in every Λ'_k and (b) to encourage smoothness in the $\lambda_{i,k}$ from ω_k to ω_{k+1} [3].

Stacking the unique unknown $\lambda'_{i,j,k}$'s (6 per frequency) into one large vector λ', I write (3.19) as;

$$C(\alpha, \lambda) = \parallel \hat{\mu}'(\alpha) - \lambda' \parallel^2_{K_{\bar{s}}} + \beta_1 \|L_{OD}\lambda'\|_2^2 + \beta_2 \|L_D \lambda'\|_2^2. \tag{3.20}$$

where $\hat{\mu}'$ is the vector of unique elements from $R(\alpha)M_k R^T(\alpha)$ over all k. The L_i are used to regularize the problem by enforcing smoothness in the spectra of the multi pole moment estimates. Specifically, L_{OD} is for off-diagonal elements, and L_D is for

diagonal elements. They are built such that

$$\|L_D\lambda\|_2^2 = \sum_{k=1}^{M}\sum_{p=1}^{3}(\lambda'_{pp}(w_k) - \lambda'_{pp}(w_{k+1}))^2 \tag{3.21}$$

$$\|L_{OD}\lambda'\|_2^2 = \sum_{k=1}^{M}(\lambda'_{12}(w_k))^2 + (\lambda'_{13}(w_k))^2 + (\lambda'_{23}(w_k))^2. \tag{3.22}$$

The regularization parameters β_i in (3.20) are used to determine the tradeoff in the reconstruction between the two terms in the cost function. The first terms enforces fidelity to the data while the second ensures smooth spectra in (3.21).

To minimize the cost function, I note first that because (3.21) is quadratic with respect to λ, $\hat{\lambda}$ can be explicitly stated in terms of α and $\hat{r_0}$ via

$$\hat{\lambda} = \left(K_{\bar{s}}^{-1} + \beta_1 L_{OD}^T L_{OD} + \beta_2 L_D^T L_D\right)^{-1} K_{\bar{s}}^{-1}\hat{\mu}' \equiv Q(\hat{r_0}, \alpha)\hat{\mu}' \tag{3.23}$$

so that I can write:

$$\hat{\alpha} = \arg\min_{\alpha} C(\hat{r}_0, \alpha, Q(\hat{r_0}, \alpha)\hat{\mu}') \tag{3.24}$$

$$\hat{\lambda} = Q(\hat{r}_0, \hat{\alpha})\hat{\mu}' \tag{3.25}$$

In our experiments I have found that C exhibits many local minima in terms of the orientation angles. Thus, I have adopted the following strategy: I first impose a coarse grid on the three dimensional space of all permitted orientation angles, then, for each α-value in the grid, the value of the cost function C is found. I use that α values with the smallest overall cost for that cell to initialize a full 3D non-linear

least squares scheme to find the final values of $\hat{\alpha}$. Using these values, I construct $\hat{\lambda}$ according to (3.25).

Chapter 4

Simulated and Real Data Results

In this chapter we first show the simulated data results for both algorithms and the comparison.Then, the real data results of both algorithm will be represented.

4.1 Simulated Data results

In the first subsection, the simulated data results are shown for Algorithm-I in the cases of sphere, spheroid, and ellipsoid objects with and without clutter. In the next section, we only present the results of Algorithm-II in the cases of ellipsoid with and without clutter.

4.1.1 Algorithm-I Analysis Results

In this section, firstly, the performance of the first estimation approach, Algorithm-I is demonstrated and analyzed under three mine shapes for the HMC objects without clutter. Next, we compare it with the baseline method in which clutter mitigation is performed by subtracting from the interior data at a fixed y, the average of the two horizontal samples taken on the boundary, under two mine shapes for the LMC objects with clutter. For the HMC case without clutter, we simulate data taken on a 10×10 grid of 100 cm ^{2} pixels by a monostatic transmit/receive system comprised of square coils 5 cm on a side. Ten frequencies logarithmically spaced between 0 and 4.3KHz are used. One corner of the grid is taken to be $(0, 0)$m while the opposite is at $(1, 1)$m.

As a first example of the HMC case, we consider a sphere mine located at $(x_0, y_0, z_0) = (0.50, 0.50, .10)$ m[1], and with radius 5cm. The medium as well as the object are taken to be non-ferrous and the conductivity of the sphere is 10^6S/m. We assume that the sphere's response can be modeled as a dipole and we the results of [1] to compute the dipole moment spectrum (DMS). The real and imaginary parts of this spectrum are shown as a solid line in Fig. 4.1. Because the sphere is rotationally invariant, for this problem there is no need to estimate the rotation angles so that the problem here reduces to determining the location and the DMS. To demonstrate the performance of

[1]Increasing depth here corresponds to increasing z

our approach, we perform 100 Monte Carlo simulations at a signal to noise ratio of 20 dB. In this case, the sample mean of the estimated object center is shown in the Table 4.1. In Fig. 4.1 the dotted lines show the sample mean of the estimated DMS with associated error bars. We see from these results that the approach is highly accurate both in terms of estimating the the position as well as the moment spectrum.

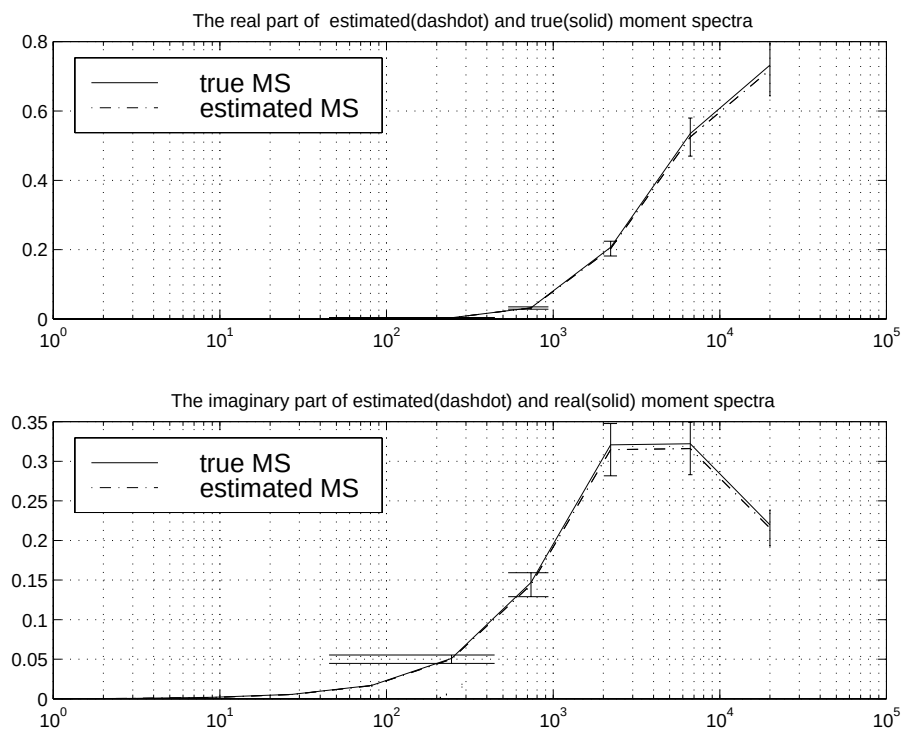

Figure 4.1: The real and imaginary part of estimated and real moment spectra of sphere mine for $\beta = 0.0001$.

As a second example, we consider a spheroidal object[2] again located at $(x_0, y_0, z_0) = (0.50, 0.50, .10)m$ and which has been rotated using $\phi = 0.75$ radians and $\psi = 2.30$

[2]Note that because the object is taken to be spheriodal, two of the three principlae axes are identical so we only need estimate a pair of rotation angles and a pair of MMS.

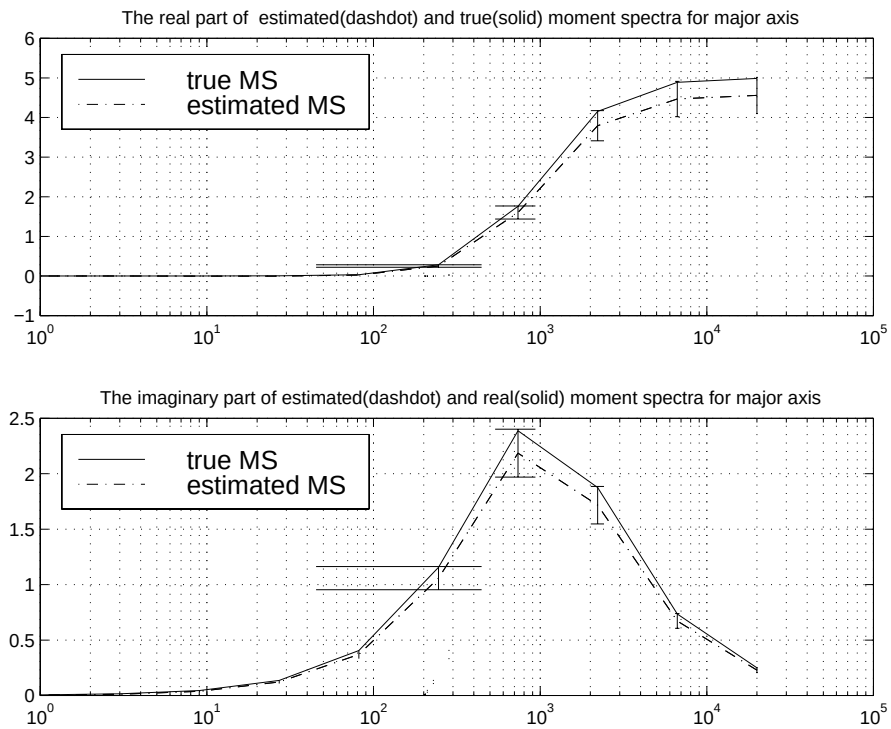

Figure 4.2: The real and imaginary part of estimated and real moment spectra of spheroid mine for $\beta_1 = 0.001$ and $\beta_2 = 0.001$, and for the major axis.

radians. In this case, we presently have no closed form expression for the frequency dependent DMS of such an object. However, under the assumption that the scattering characteristics of an eccentric object will be substantially differerent for the major versus minor axes, we hypotheses DMS spectra shown in Fig.4.2 and Fig.4.3 as solid lines and examine the performance of our approch under these conditions.

In this case, we estimate the center of object, minor and major moment spectras and two rotation angles. For spheroid object, we assume that the optimum β_1 and β_2 values for the major and minor axis are known. For $\beta_1 = 0.001$ and $\beta_2 = 1$,

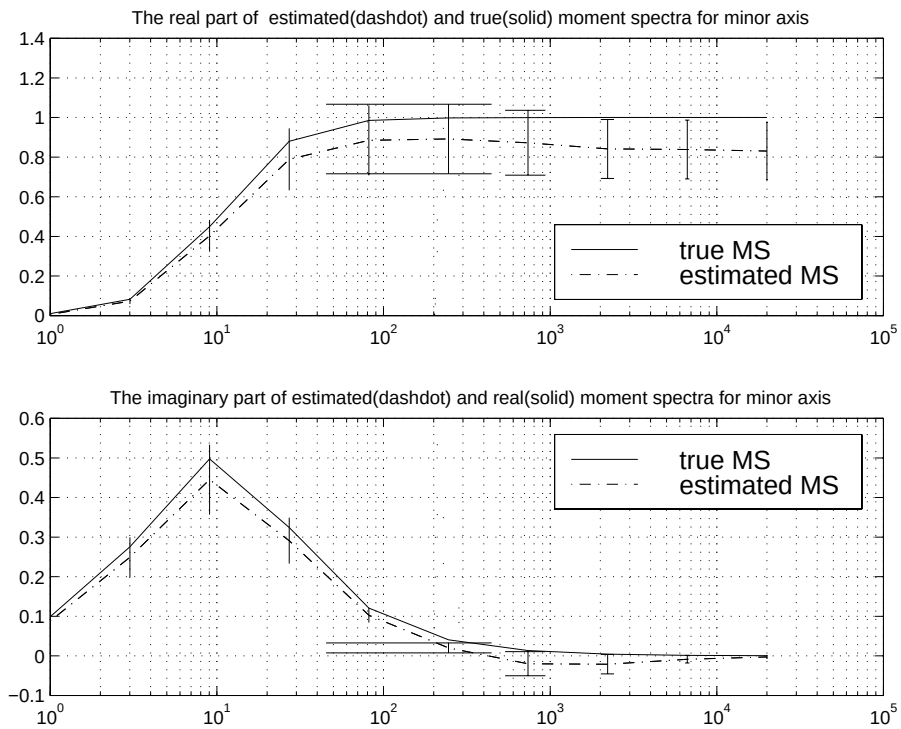

Figure 4.3: The real and imaginary part of estimated and real moment spectra of spheroid mine for $\beta_1 = 0.001$ and $\beta_2 = 1$, and for the minor axis.

after performing 100 Monte Carlo simulations at 20 SNR, the sample mean of the estimated object center is shown in the Table 4.1. The sample mean of estimated rotation angles are also shown in this table. The real and imaginary parts of two estimated with errorbar and real moment spectras for major and minor axis are shown in Fig.4.2 and Fig.4.3, respectively

As a last example for the data without clutter, we consider an ellipsoid object at the same location as the previous examples. For this case the data that we will use is same as the data that we used for the second example, spheroid case. For $\beta_1 = 0.001$,

	Sphere		Spheroid		Ellipsoid	
	mean	Standard Deviation	mean	Standard Deviation	mean	Standard Deviation
$\hat{x}_0$	0.5000	0.0002	0.5003	0.0021	0.5002	0.0014
$\hat{y}_0$	0.5001	0.0002	0.4996	0.0015	0.5007	0.0017
$\hat{z}_0$	0.0999	0.0010	0.0971	0.0046	0.0925	0.0061
$\hat{\phi}$	-	-	0.7541	0.0354	0.7571	0.2991
$\hat{\psi}$	-	-	2.3411	0.0805	2.5533	0.0972
$\hat{\theta}$	-	-	-	-	0.0515	0.2652

Table 4.1: The estimated object center and rotation angle results for Algorithm-I

$\beta_2 = 0.001$ and $\beta_3 = 1$, after we perform 100 Monte Carlo simulations at 20 SNR for this case, the sample mean of the estimated object center and the sample mean of estimated rotation angles are represented in the Table 4.1. The real and imaginary parts of two estimated with errorbar and real moment spectras for first, second and third axis are shown in Fig.4.4, Fig.4.5 and Fig.4.6, respectively. From Fig.4.4 and Fig.4.5 we see that their MS estimations are approximately same.

All the sample mean of the estimated object center and rotation angeles for three examples are illustrated in the Table 4.1 with standard deviations. From all results the approach estimating the position, the rotation angle and the momemt spectrum is highly precise.

For the data containg LMC objects with clutter, we simulate data taken on a 9×9 grid of 81 cm ^{2} pixels by a monostatic transmit/receive system comprised of square coils 5 cm on a side. Ten frequencies logarithmically spaced between 0 and 4.3kHz

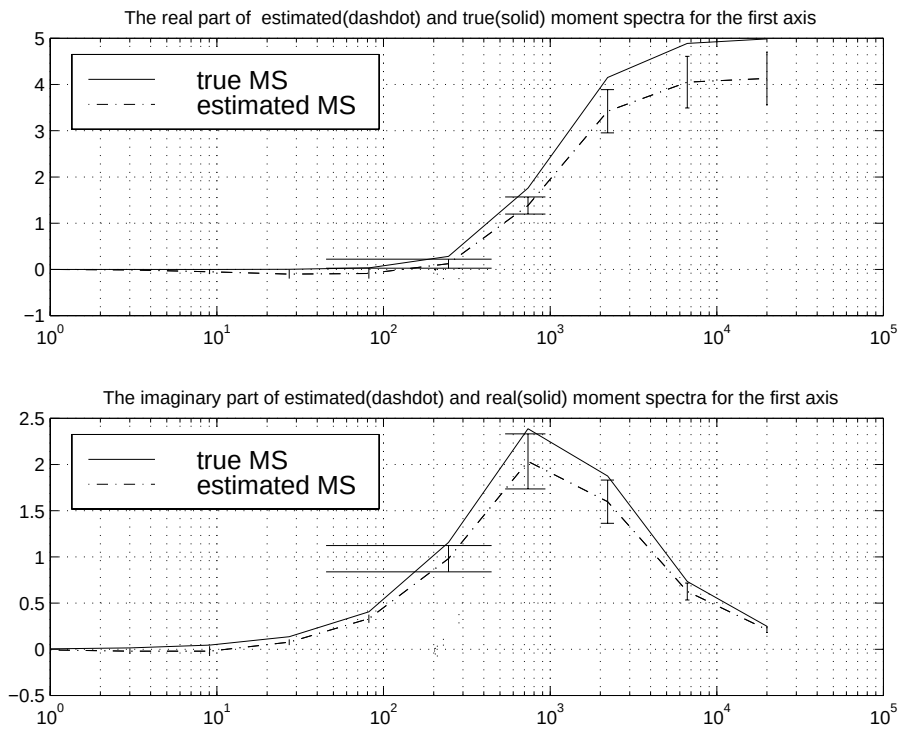

Figure 4.4: The real and imaginary part of estimated and real moment spectra of spheroid mine for $\beta_1 = 0.001$, $\beta_2 = 0.001$ and $\beta_3 = 1$, and for the first axis.

are used. One corner of the grid is taken to be $(-0.4, -0.4)$m while the opposite is at $(0.4, 0.4)$m.

As a first example of the LMC case, we consider a sphere mine located at $(x_0, y_0, z_0) = (0, 0, .10)$m, and with radius 5cm. The medium as well as the object are taken to be non-ferrous. The real and imaginary parts of this spectrum are shown as a solid line in Fig. 4.7. Because the sphere is rotationally invariant, for this problem there is no need to estimate the rotation angles so that the problem here reduces to determining the location and the DMS. To demonstrate the performance of our approach, we

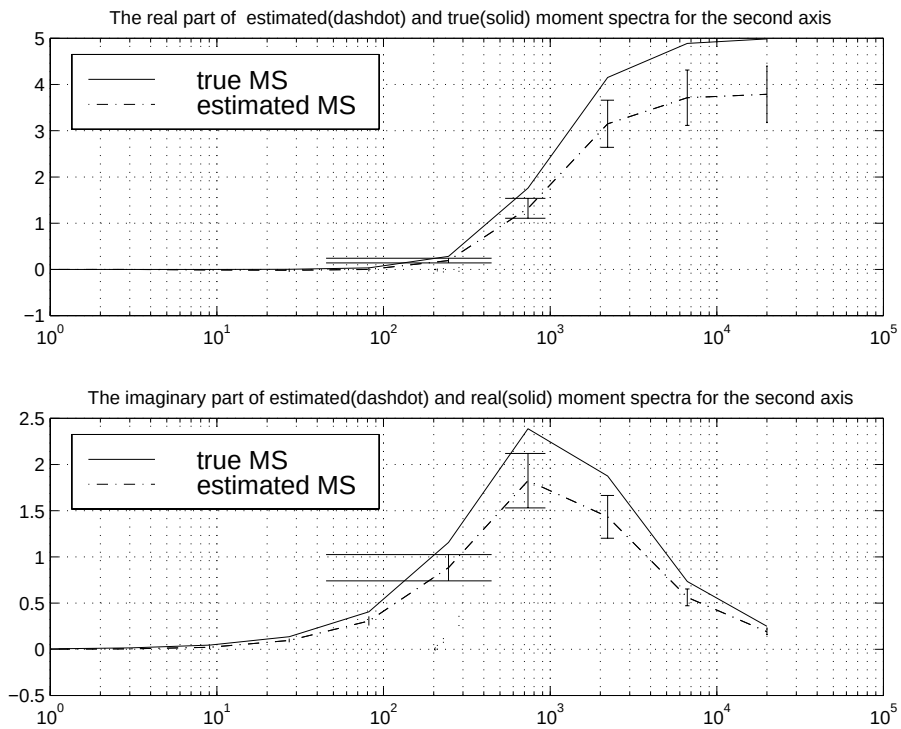

Figure 4.5: The real and imaginary part of estimated and real moment spectra of spheroid mine for $\beta_1 = 0.001$, $\beta_2 = 0.001$ and $\beta_3 = 1$, and for the second axis.

perform 100 Monte Carlo simulations at a signal to clutter plus noise ratio(SCNR) of 20 dB. The sample mean of the estimated object center is shown in the Table 4.2 for our model and the baseline method with a standard deviation. In Fig. 4.14 the dotted lines show the sample mean of the estimated DMS according to both methods. We see from these results that our approach is highly accurate and better when compared with the baseline method both in terms of estimating the position as well as the moment spectrum.

As a second example, we consider an ellipsoid object again located at $(x_0, y_0, z_0) =$

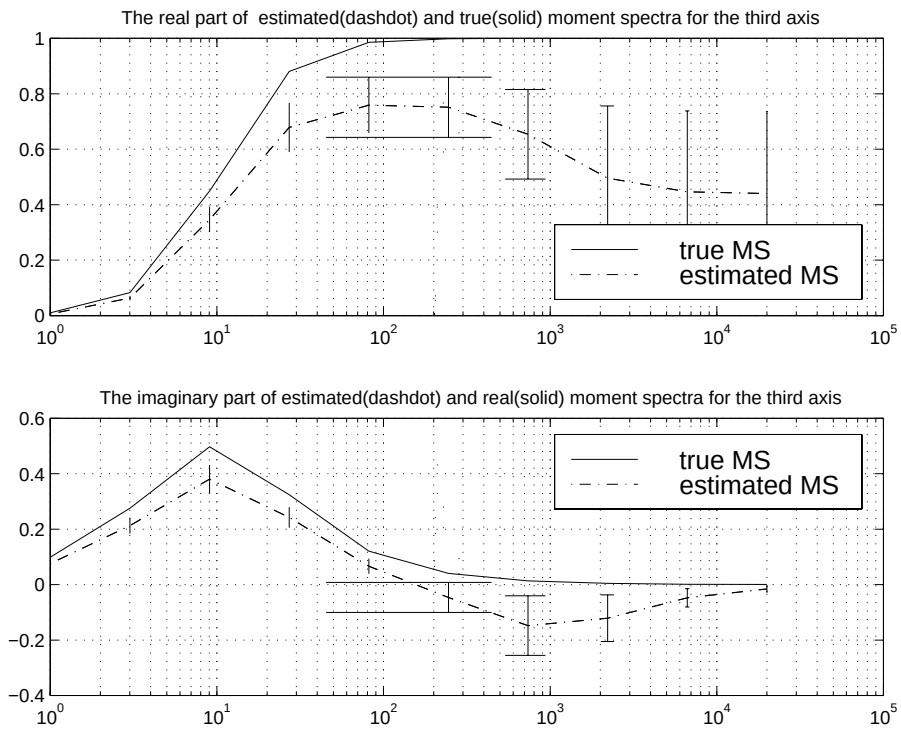

Figure 4.6: The real and imaginary part of estimated and real moment spectra of spheroid mine for $\beta_1 = 0.001$, $\beta_2 = 0.001$ and $\beta_3 = 1$, and for the third axis.

$(0, 0, .10)$m and which has been rotated using $\phi = 1.50$ radians, $\psi = 1.50$ radians and $\theta = 1.90$ radians. In this case, we presently have no closed form expression for the frequency dependent DMS of such an object. However, under the assumption that the scattering characteristics of an eccentric object will be substantially different among axes, we hypotheses DMS spectra shown in Fig. 4.8, Fig. 4.9, and Fig. 4.10 as solid lines and examine the performance of our approach under these conditions.

In this case, we estimate the center of object, moment spectra for three axes and three rotation angles. For ellipsoid object, we assume that the optimum β_1 and β_2

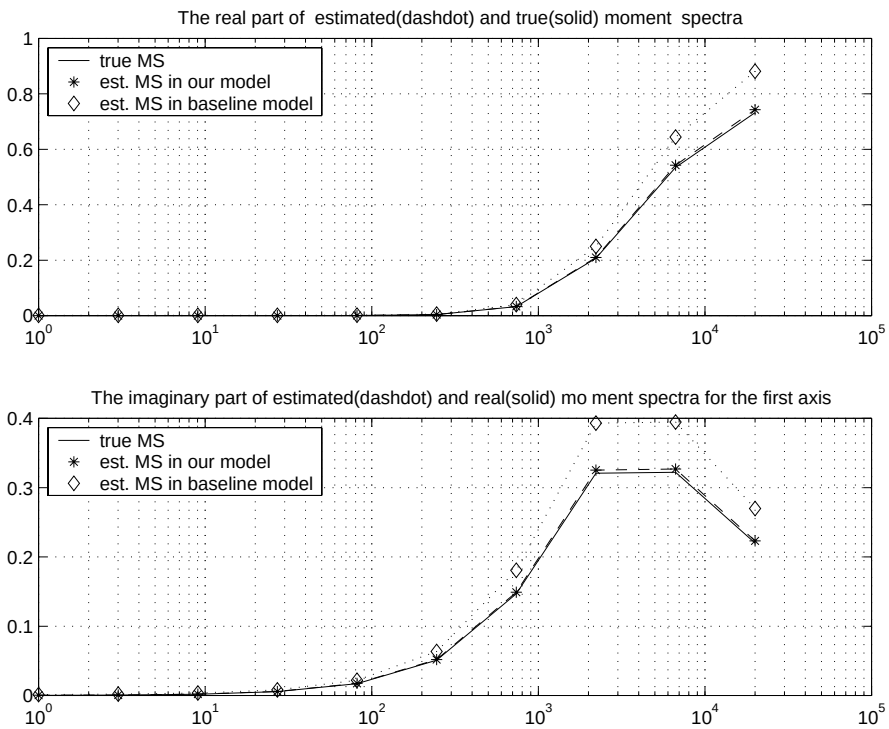

Figure 4.7: The real and imaginary part of estimated and real moment spectra of sphere mine

values for the major and minor axis are known. After performing 100 Monte Carlo simulations at 20 SCNR, all results for both models are represented in the Table 4.2. The real and imaginary parts of two estimated and real moment spectra all axes according to both models are shown in Fig. 4.8– 4.10.

All the sample mean of the estimated object center and rotation angles for two examples are illustrated in the Table 4.2 with standard deviations according to both models. From all results our approach estimating the position, the rotation angle and the moment spectrum is highly precise and we can say that it is much better than

	Sphere Case				Ellipsoid Case			
	Our Model		Baseline Model		Our Model		Baseline Model	
	mean	Standard Deviation	mean	Standard Deviation	mean	Standard Deviation	mean	Standard Deviation
$\hat{x}_0$	-0.0001	0.0002	0.0042	0.0103	-0.0000	0.0001	0.0066	0.0111
$\hat{y}_0$	-0.0009	0.0005	-0.0074	0.0042	0.0001	0.0003	-0.0059	0.0075
$\hat{z}_0$	0.1002	0.0004	0.1149	0.0194	0.1001	0.0009	0.9740	0.0097
$\hat{\phi}$	-	-	-	-	1.6991	0.0033	1.6328	0.0061
$\hat{\psi}$	-	-	-	-	1.7025	0.0037	1.7842	0.0101
$\hat{\theta}$	-	-	-	-	1.8705	0.0041	2.1993	0.0140

Table 4.2: The estimated object center and rotation angle results according to our model and baseline model.

the baseline model for the certain of the moment spectras.

4.1.2 Algorithm-II Analysis Results

In this section, we first demonstrate and analyze the performance of the parameter estimation of the second processing approach, Algorithm-II for one mine shape for the HMC objects without clutter. Then, we compare it for two mine shapes for the LMC objects with clutter to that of a baseline method. Finally, we do the comparison of two algorithms. The simulate datum for the following simulations are same as the previous section's.

As an example for the HMC data without clutter, we consider an ellipsoid object at the same location as the previous examples. For $\beta_1 = 10^{-6}$, $\beta_2 = 10^{-3}$ and $\beta_3 = 10^{-6}$, after we perform 100 Monte Carlo simulations at 30 SNR for this case, the sample

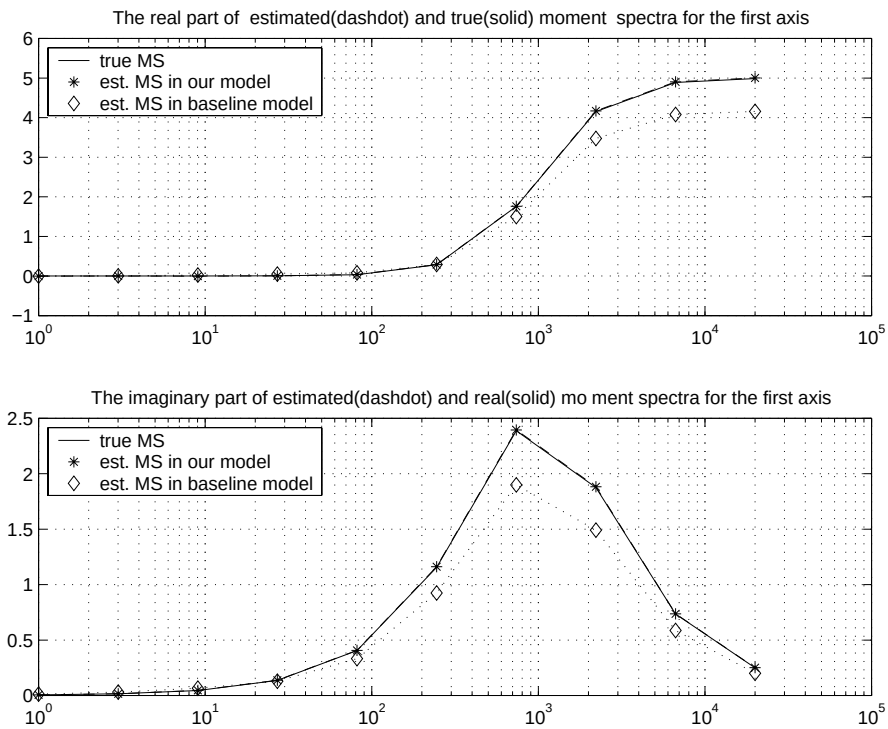

Figure 4.8: The real and imaginary part of estimated and real moment spectra of spheroid mine for the first axis.

mean of the estimated object center is $(0.5001, 0.4989, 0.0909)m$ with a standard deviation of $\pm(0.0027, 0.0042, 0.0139)$. The sample mean of estimated rotation angles are $\phi = 1.5693$ radians, $\psi = 1.5665$ and $\theta = 1.5751$ radians with standard deviations of $\pm(0.0628)$, $\pm(0.0327)$ and $\pm(0.1743)$ respectively. The real and imaginary parts of two estimated with errorbar and real moment spectras for first, second and third axis are shown in Fig.4.11, Fig.4.12 and Fig.4.13, respectively. From Fig.4.12 and Fig.4.13 we see that their MS estimations are approximately same.

As a first example of LMC case, we consider a sphere mine located at $(x_0, y_0, z_0) =$

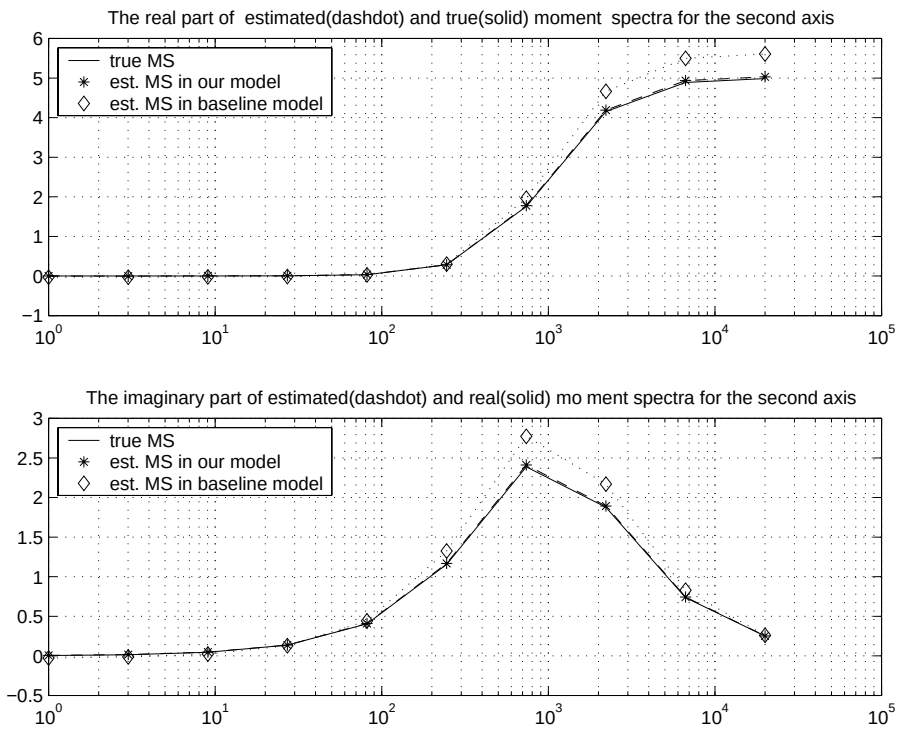

Figure 4.9: The real and imaginary part of estimated and real moment spectra of spheroid mine for the second axis.

$(0, 0, .10)$m, and with radius 5cm. Because the sphere is rotationally invariant, for this problem there is no need to estimate the rotation angles so that the problem here reduces to determining the location and the DMS. To demonstrate the performance of our approach, we perform 100 Monte Carlo simulations at a signal to interference plus noise ratio(SCNR) of 10 dB. In our model, the sample mean of the estimated object center is $(-0.0004, -0.0009, 0.1017)$m with a standard deviation of $\pm(0.0003, 0.0010, 0.0021)$m. In the baseline method, it is $(0.0237, -0.0059, 0.1144)$ with a standard deviation of $\pm(0.0156, 0.0035, 0.0123)$m. In Fig. 4.14 the dotted lines

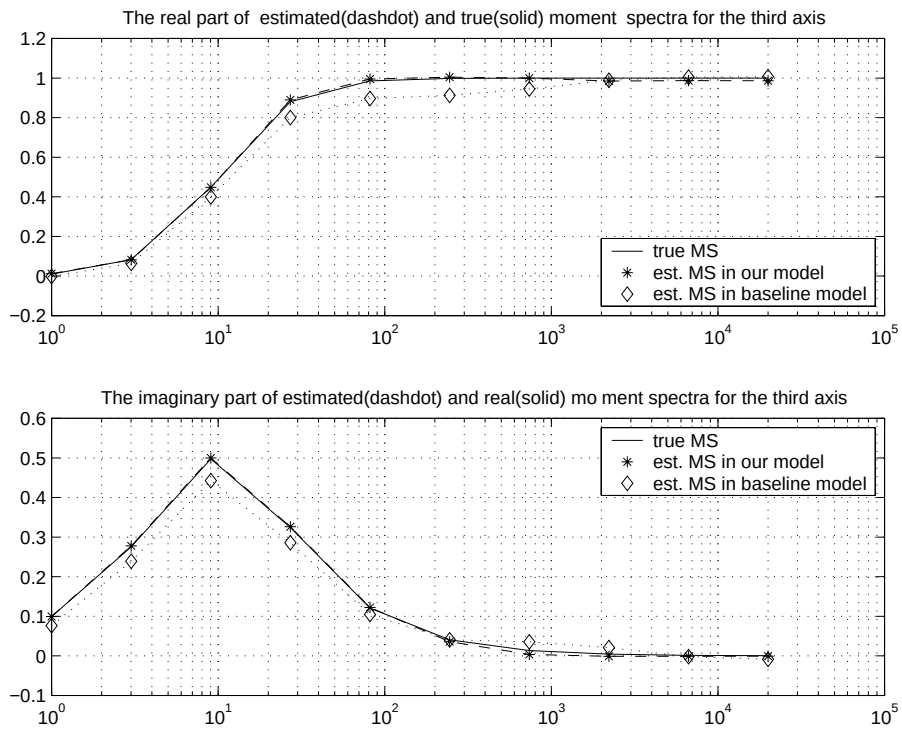

Figure 4.10: The real and imaginary part of estimated and real moment spectra of spheroid mine for the third axis.

show the sample mean of the estimated DMS according to both methods. We see from these results that our approach is highly accurate and better when compared with the baseline method both in terms of estimating the position as well as the moment spectrum.

As a second example, we consider an ellipsoid object again located at $(x_0, y_0, z_0) = (0, 0, .10)$m and which has been rotated using $\phi = 1.70$ radians, $\psi = 1.70$ radians and $\theta = 1.70$ radians. In this case, we presently have no closed form expression for the frequency dependent DMS of such an object. However, under the assumption that the

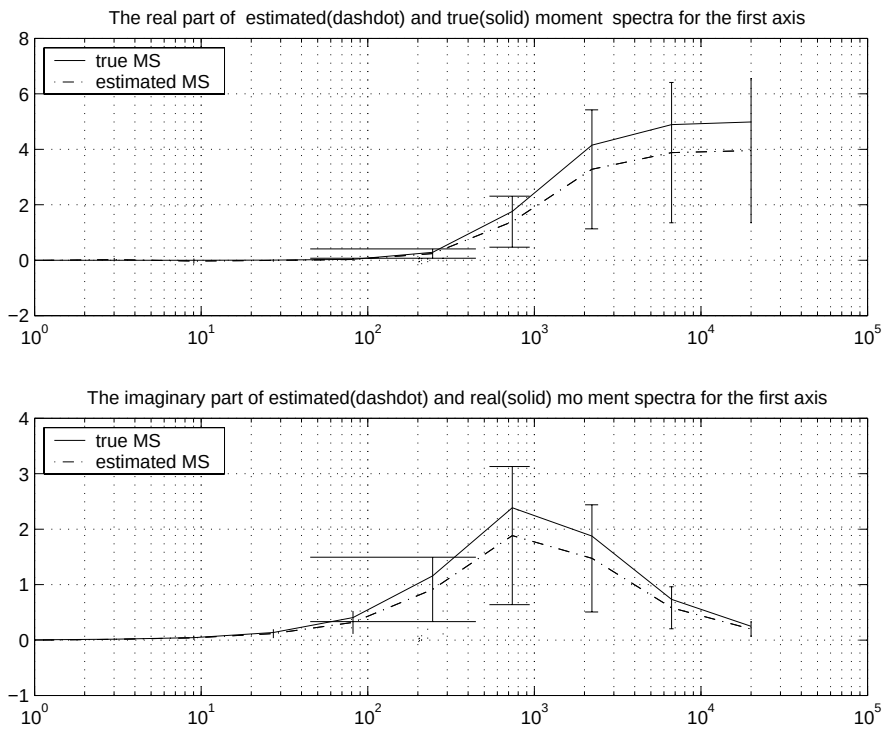

Figure 4.11: The real and imaginary part of estimated and real moment spectra of spheroid mine for the first axis.

scattering characteristics of an eccentric object will be substantially different among axes, we hypotheses DMS spectra shown in Fig. 4.15, Fig. 4.16, and Fig. 4.17 as solid lines and examine the performance of our approach under these conditions.

In this case, we estimate the center of object, moment spectra for three axes and three rotation angles. For ellipsoid object, we assume that the optimum β_1 and β_2 values for the major and minor axis are known. After performing 100 Monte Carlo simulations at 10 SCNR, in our model the sample mean of the estimated object center is $(-0.0005, 0.0001, 0.0985)$m with a standard deviation of $\pm(0.0004, 0.0003, 0.0012)$m,

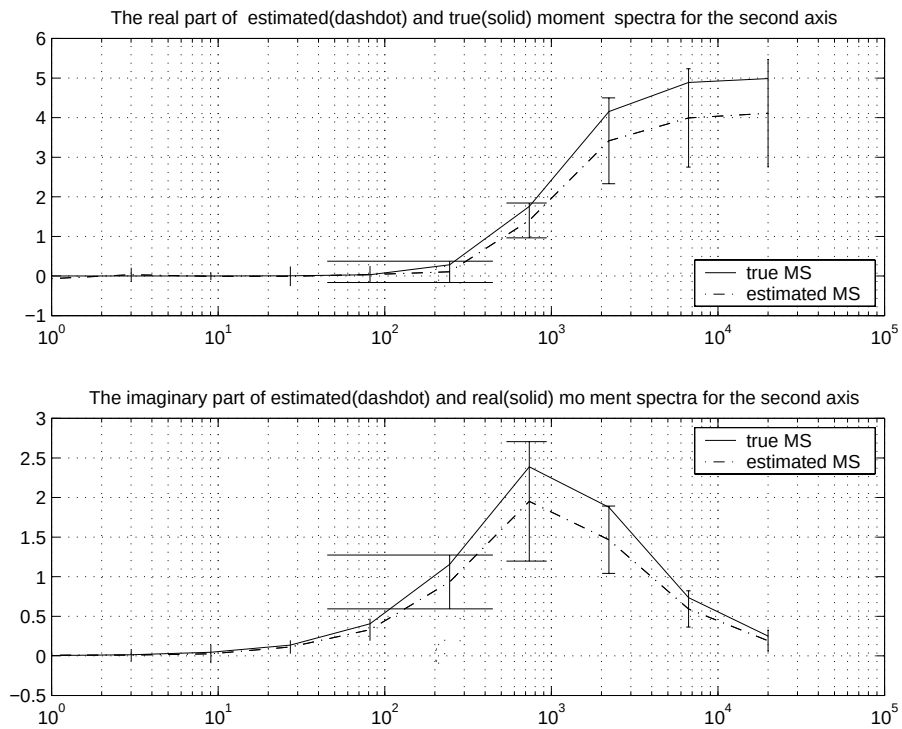

Figure 4.12: The real and imaginary part of estimated and real moment spectra of spheroid mine for the second axis.

and in baseline model $(0.0578, -0.0011, 0.1107)$m with a standard deviation of $\pm(0.0562, 0.0025, 0.0129)$m. The sample mean of estimated rotation angles in our model are $\phi = 1.66751$ radians, $\psi = 1.7163$ radians, and $\theta = 1.9097$ radians with standard deviations of $\pm(0.0041)$, $\pm(0.0014)$, and $\pm(0.0073$, respectively, and in the other model $\phi = 1.5050$ radians, $\psi = 1.2052$ radians, and $\theta = 2.7402$ radians with standard deviations of $\pm(0.072)$, $\pm(0.0371)$, and $\pm(0.0053)$, respectively. The real and imaginary parts of two estimated and real moment spectra all axes according to both models are shown in Fig. 4.15– 4.17.

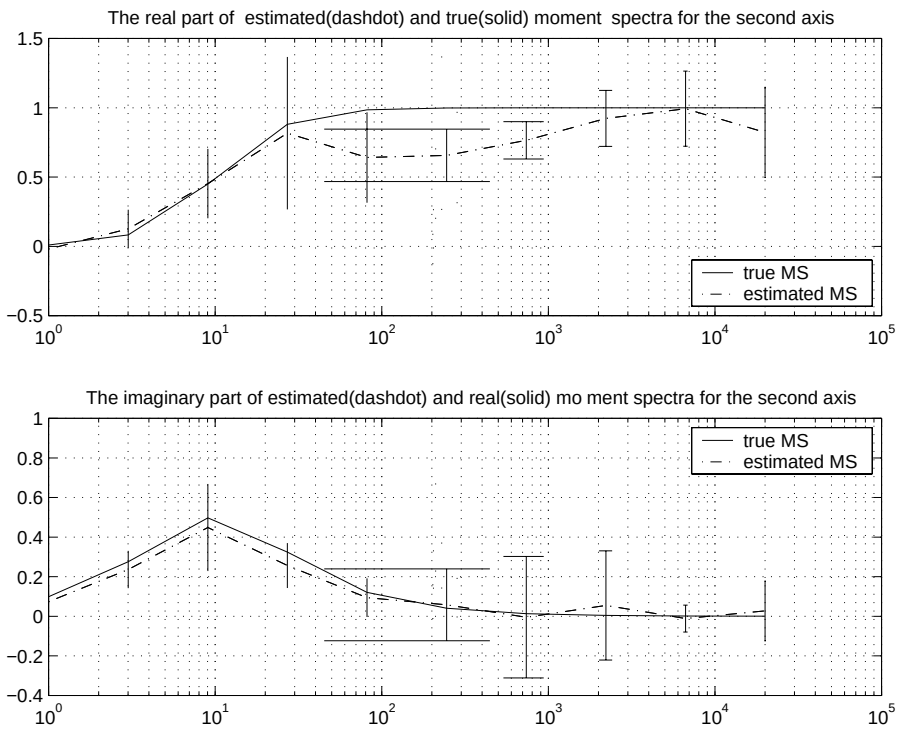

Figure 4.13: The real and imaginary part of estimated and real moment spectra of spheroid mine for the third axis.

The following two tables summarize the comparison of two algorithms. The first Table 4.3 compares the estimated object center for the sphere and ellipsoid cases. The real object center is $(0, 0, 0.1)m$. For the ellipsoid case it also shows the estimated orientation angles compared the real ones,$(2.4, 2.4, 2.4)radians$.

The second Table 4.4 compares the average run time and MSE values for MMS, object center, and orientation angles for the sphere and ellipsoid case. The average times of both algorithm are close to each other for the sphere case but the Algorithm-II's is much faster than the Algorithm-I's for the ellipsoid case. However, the Algorithm-I

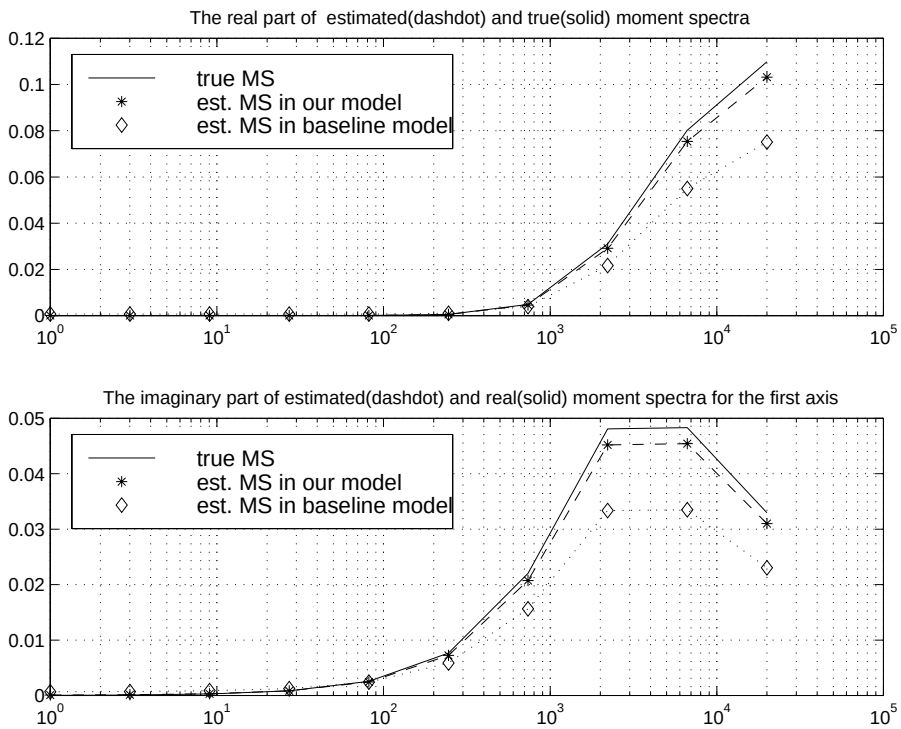

Figure 4.14: The real and imaginary part of estimated and real moment spectra of sphere mine

is much better than the algorithm-II for the other values. In other words, there is a trade-off between the speed and the performance of the Algorithm-II but the reverse analogy for the Algorithm-I for the case of ellipsoid objects.

4.2 Real Data Results

In this section, we represent the real data results for both algorithms. The first data set is from GEM-3 sensor of Geophex company and second data set is obtained from the Northeastern University CER. We use the first data set for Algorithm-I and the

	Sphere Case				Ellipsoid Case			
	Algorithm-I		Algorithm-II		Algorithm-I		Algorithm-II	
	mean	Standard Deviation	mean	Standard Deviation	mean	Standard Deviation	mean	Standard Deviation
$\hat{x}_0$	0.0000	0.0011	0.0002	0.0011	0.0001	0.0061	0.0016	0.0110
$\hat{y}_0$	-0.0000	0.0012	-0.0001	0.0010	0.0002	0.0054	-0.0006	0.0102
$\hat{z}_0$	0.0999	0.0014	0.0906	0.0049	0.1011	0.0115	0.1018	0.0181
$\hat{\phi}$	-	-	-	-	2.4867	0.5138	2.4882	0.8550
$\hat{\psi}$	-	-	-	-	2.4765	0.4322	2.0500	0.5688
$\hat{\theta}$	-	-	-	-	2.3639	0.1935	2.3492	0.7515

Table 4.3: Comparison of Algorithm-I and Algorithm-II according to location center and rotation angles

	Sphere Case		Ellipsoid Case	
	Algorithm-I	Algorithm-II	Algorithm-I	Algorithm-II
Avg Time	43.3322	53.1447	245.2957	157.7345
MSE for λ	0.0044	0.3632	4.6625	4.6943
MSE for r0	0.0001	0.0094	0.0012	0.0025
MSE for α	-	-	0.1868	0.3303

Table 4.4: Comparison of Algorithm-I and Algorithm-II according to the average run time and MSE values for all variables.

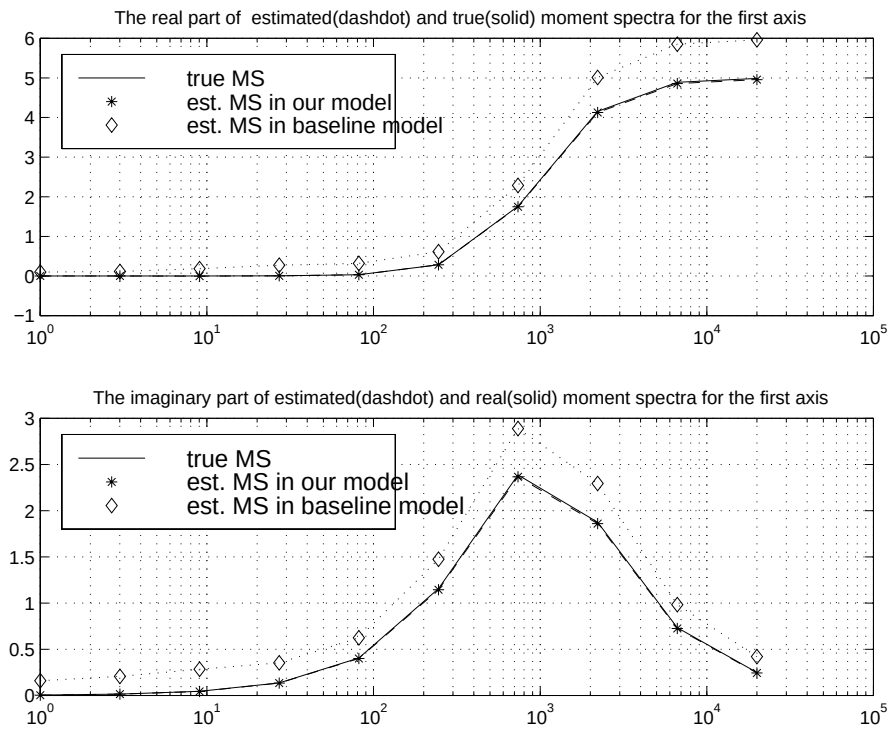

Figure 4.15: The real and imaginary part of estimated and real moment spectra of spheroid mine for the first axis.

second one for both algorithms and baseline method for comparison.

In the first data set, the GEM-3 specifications are in the following: the sphere diameters are 5.1cm; the cylinder diameters are 3.2cm and their lengths are 7.6cm. The censor coil parameters are: transmit coil radius is 24.0cm (the number of turns is 14), the bucking coil radius is 13.3cm (the number of turns is 7), and the receiving coil radius is 7.5cm. The frequencies used in the data are: 30, 90, 150, 210, 330, 390, 570, 750, 990, 1290, 1770, 2370, 3150, 4170, 5610, 7470, 10050, 13410, 17910, 23970. The data were recorded on a 7×7 grid of 100 cm ^{2} pixels. The cylinder data were

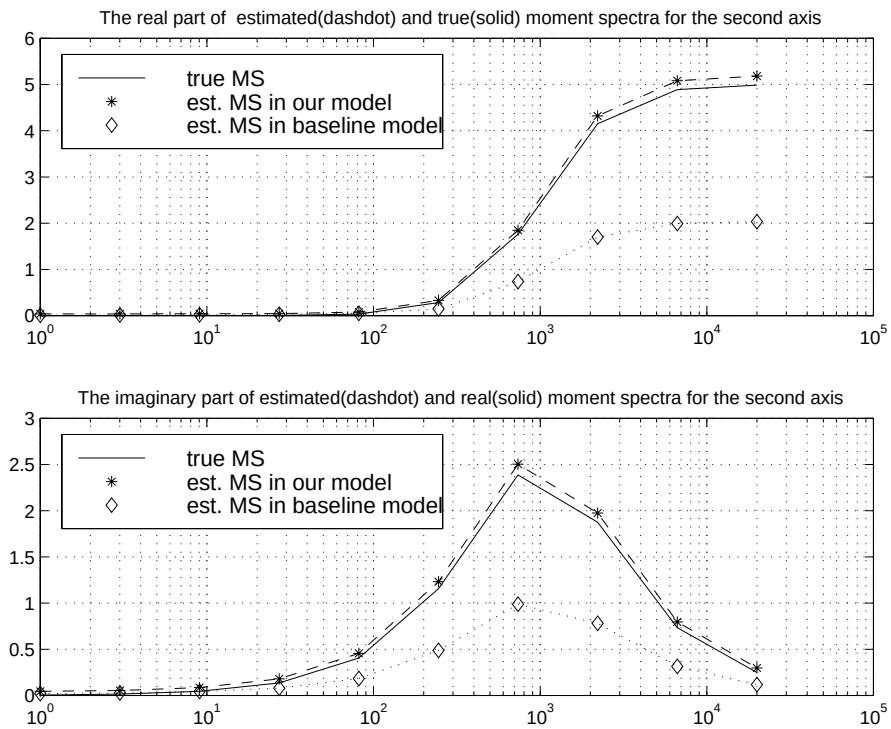

Figure 4.16: The real and imaginary part of estimated and real moment spectra of spheroid mine for the second axis.

taken for steel, aluminum and brass at three orientations in a hole in the ground. The stand-off distance is 12.5cm for the vertical and 45 degree orientations and 15cm for the horizontal case. The stand-off distances indicated are measured from the bottom of the sensor to the closest point on the cylinder for all orientations.

The figures, 4.18, 4.19, 4.20, 4.22, 4.23, 4.24, 4.25, 4.26, 4.27, show DMS results of GEM-3 data from Geophex company. Specifically, the figures, 4.18, 4.19, and 4.20 show the DMS of the cylindrical aluminum object for three axes according to Algorithm-I. The figures, 4.22, 4.23, and 4.24 show the DMS of the cylindrical

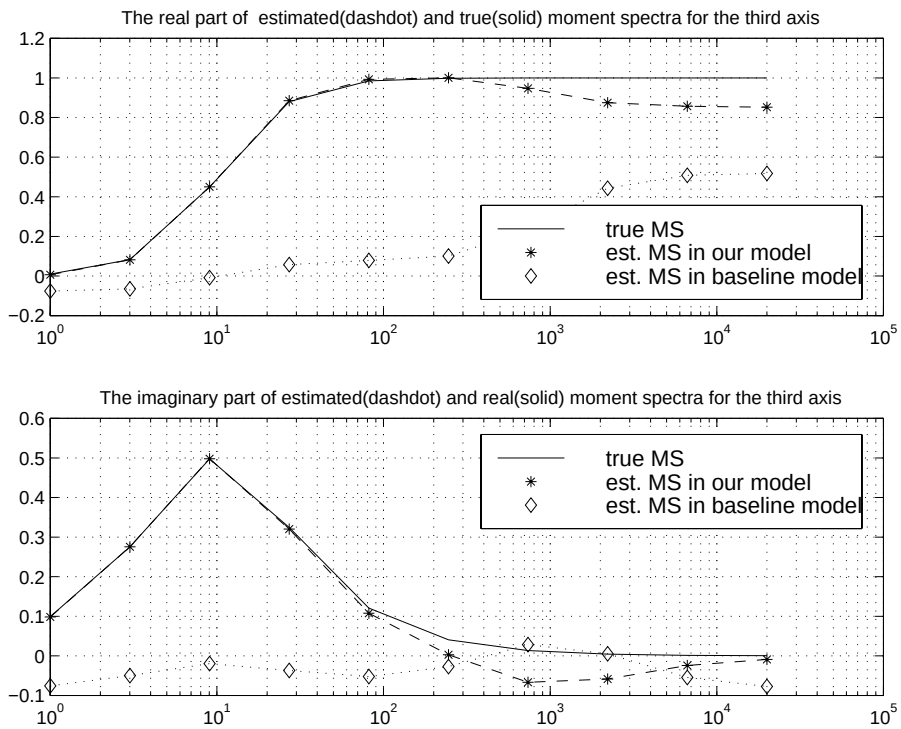

Figure 4.17: The real and imaginary part of estimated and real moment spectra of spheroid mine for the third axis.

brass object for three axes. The other three figures, , 4.25, 4.26,and 4.27 represent the results for the cylindircal steel object. The estimated locations of the steel object are $(0.01, 0.01, 0.1094)$, $(0.01, 0.01, 0.1795)$, and $(0.01, 0.01, 0.1452)$ compared with the real locations, $(0, 0, 0, 125)$, $(0, 0, 0.15)$, and $(0, 0, 0.125)$ for the cases of vertical, horizontal, and 45-degrees, respectively.

As seen from these figures, one of the most important results is that the DMS estimation is invariant to orientation change, that is, no matter how the object is put, such as, in a vertical, horizontal or 45 degree way in this real data, we get the

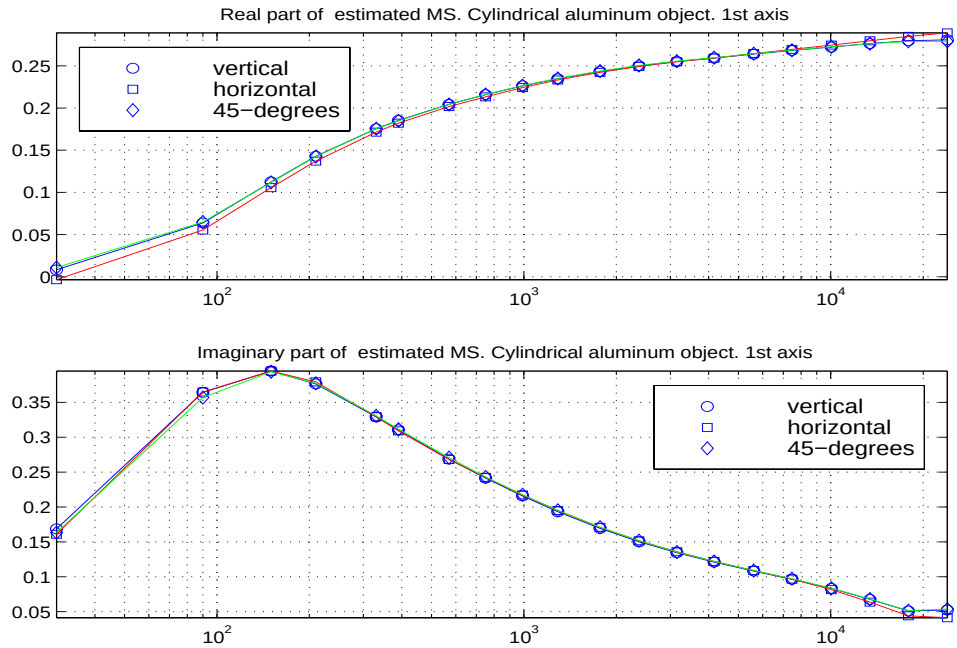

Figure 4.18: The real and imaginary part of estimated DMS of cylindrical aluminum object for the first axis according to Algorithm-I.

same DMS estimate for each axis. According to our model, we are supposed to have the same DMS estimate for the sphere object and two the same for cylinders and spheroidal type targets. Therefore, the other very important result is that we got two same DMS estimates for aluminum, brass and steel cylindrical objects. Especially, for the steel case two DMS are same and the third axis one is clearly different than the other two.

As a second data we use the data set for Northeastern University Magnetic Researche Center.The data specifications are same as GEM-3 mentioned before. For this data set, the first step is that after we removed the clutter data from the signal

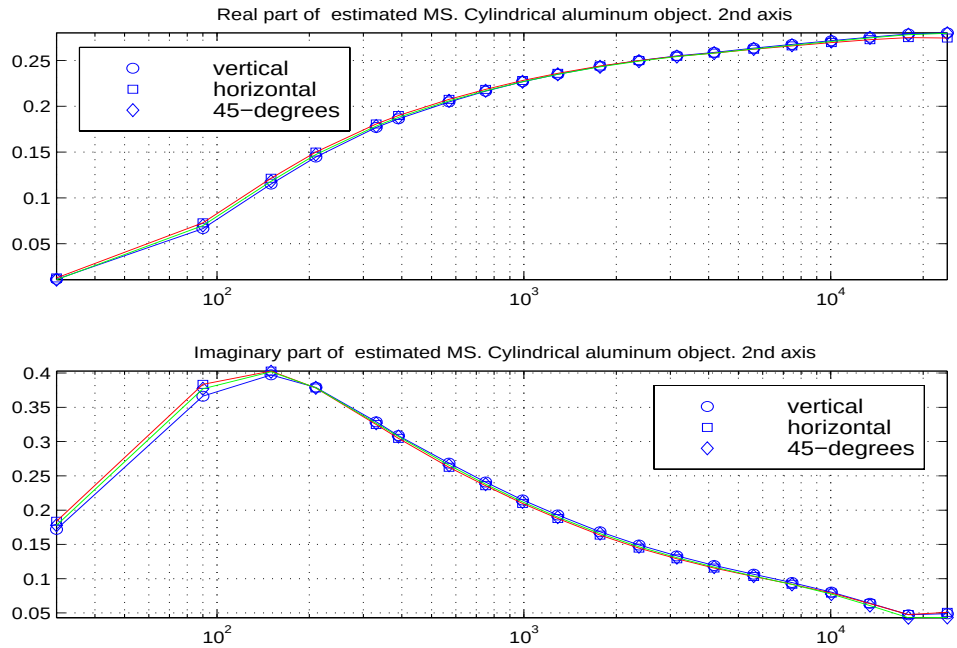

Figure 4.19: The real and imaginary part of estimated DMS of cylindrical aluminum object for the second axis according to Algorithm-I.

data, we estimated the object center and then the DMS of each object for each axis according to Algorithm-I. The solid line in the following figures, 4.28, 4.29, 4.30, 4.31, 4.32, 4.33, 4.34, 4.35, 4.36, 4.37, 4.38, and 4.39, shows the results of DMS estimates using Algorithm-I. Then, we added clutter and noise to the data and we applied Algorithm-II to obtain the DMS estimates together with our model and and the baseline model to get rid of the clutter, and we got the other two lines with star and diamond. All these steps are outlined in the following flowchart, 4.21. The first three figures, 4.28, 4.29, and 4.30 show the results for aluminum object.The figures, 4.31, 4.32, and 4.33, is for striker object and 4.34, 4.35,and 4.36 for val69

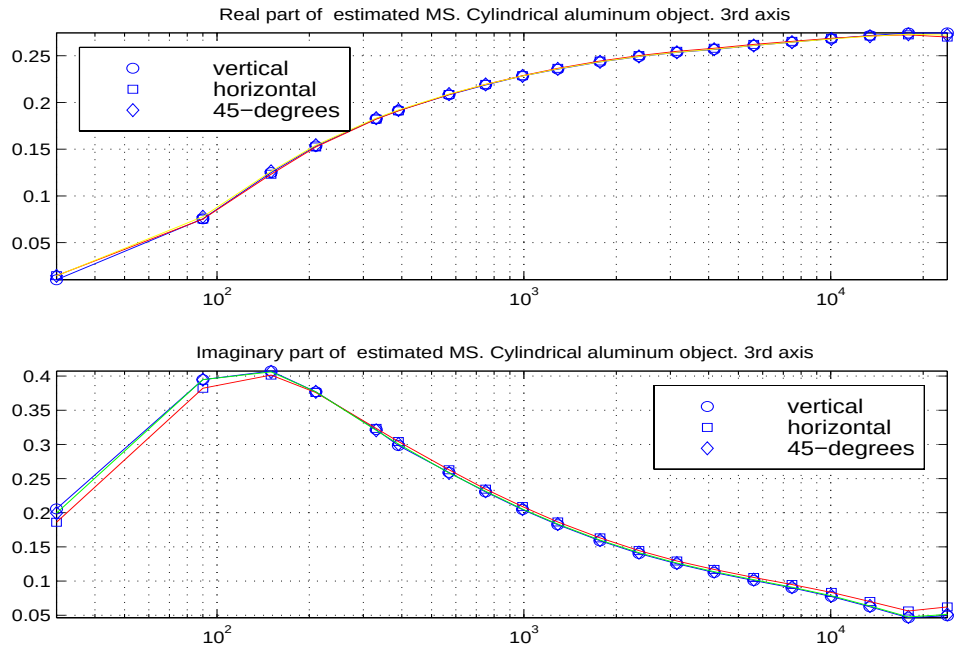

Figure 4.20: The real and imaginary part of estimated DMS of cylindrical aluminum object for the third axis according to Algorithm-I.

mine, and 4.37, 4.38, and 4.39 for vs50 mine.

Apparently, we can easily compare all methods in these figures. Although we are not sure about the real DMS, we can say that the solid lines in the figures are the closest estimate since they are results of the cleaner data than the others. The ones with star are closer to the solid lines than the ones with diamond so our model works better than the baseline model.

Finally, we played the game of adding sensor noise similar to the previous case. After cleaning the real data, we determined the DMS of the object using Algorithm-I, shown as a solid line in the previous figures. Then, using these DMS, we made the

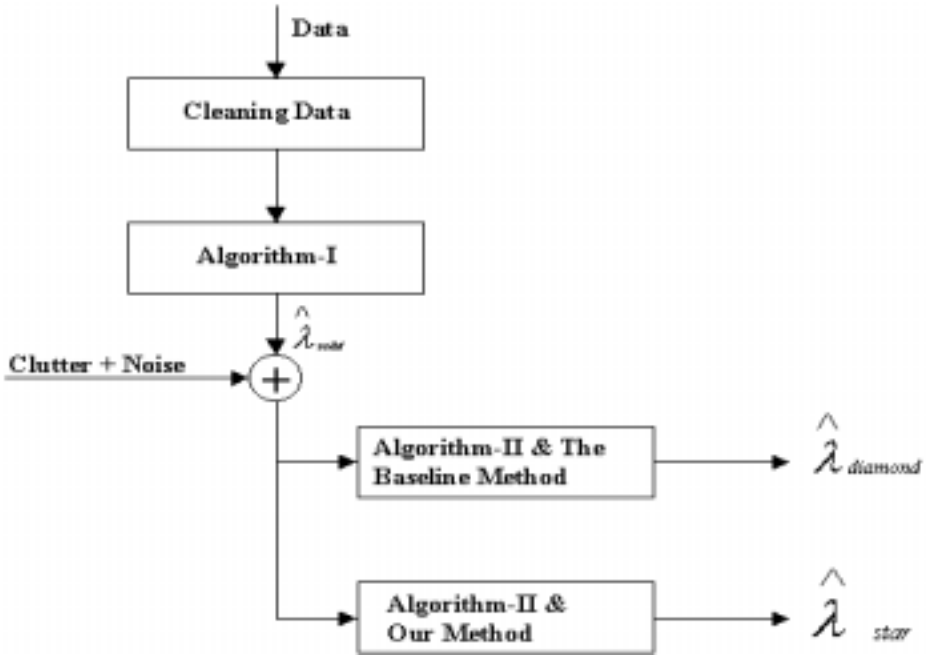

Figure 4.21: Flowchart for the second data.

noisy signal data. Next we reestimated the DMS and we calculated the mean square errors between the latter DMS and the former DMS's. We performed 100 Monte Carlo simulations for each case. Our goal here is that we want to see how well we can classify using Alg-I. The results are shown in the following Table 4.5:

As final figures, the figures, 4.40, and 4.41 show the comparison of two algorithms

	Aluminum	Striker	Val69	Vs50
Aluminujm	0.72	0.07	0.00	0.21
Striker	0.02	0.90	0.06	0.02
Vs50	0.15	0.04	0.00	0.81
Val69	0.00	0.04	0.96	0.00

Table 4.5: The classification results

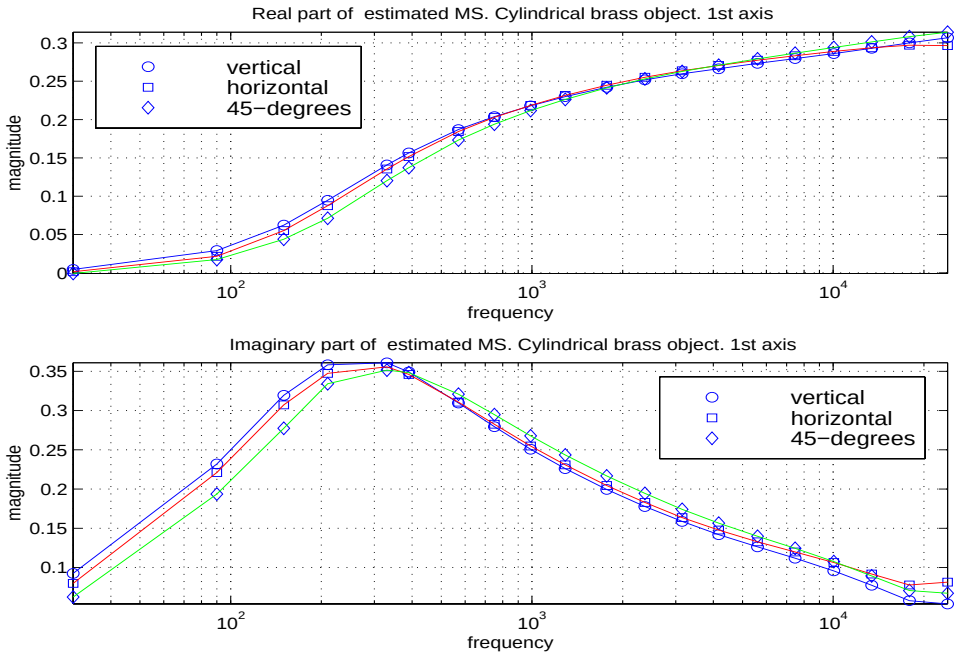

Figure 4.22: The real and imaginary part of estimated DMS of cylindrical brass object for the first axis according to Algorithm-I.

for the estimation of DMS. It is obtained by using the GEM-3 data. As seen from figures, we get almost same results from both algorithms.

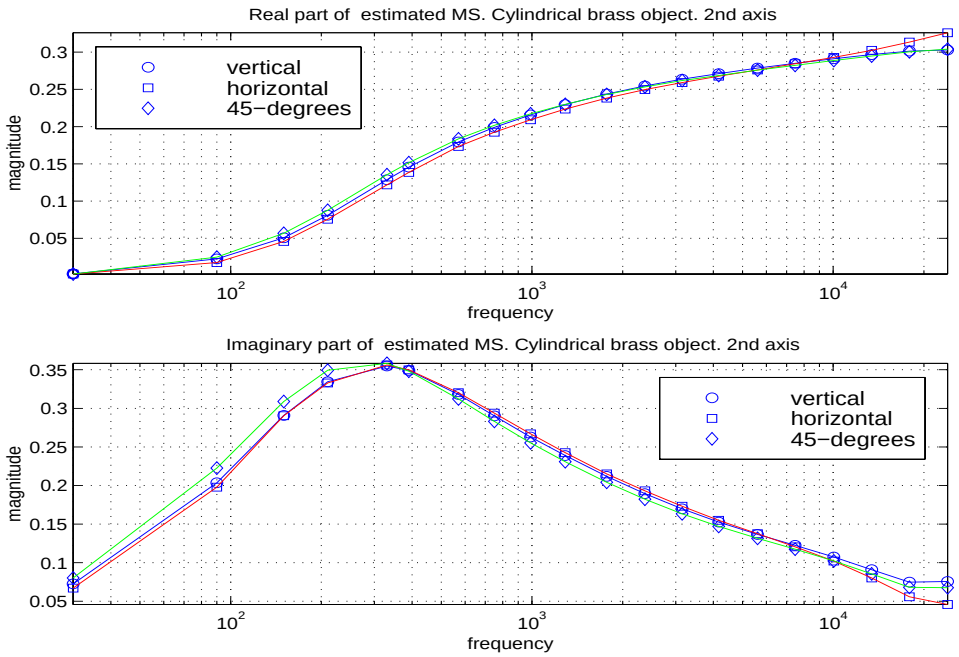

Figure 4.23: The real and imaginary part of estimated DMS of cylindrical brass object for the second axis according to Algorithm-I.

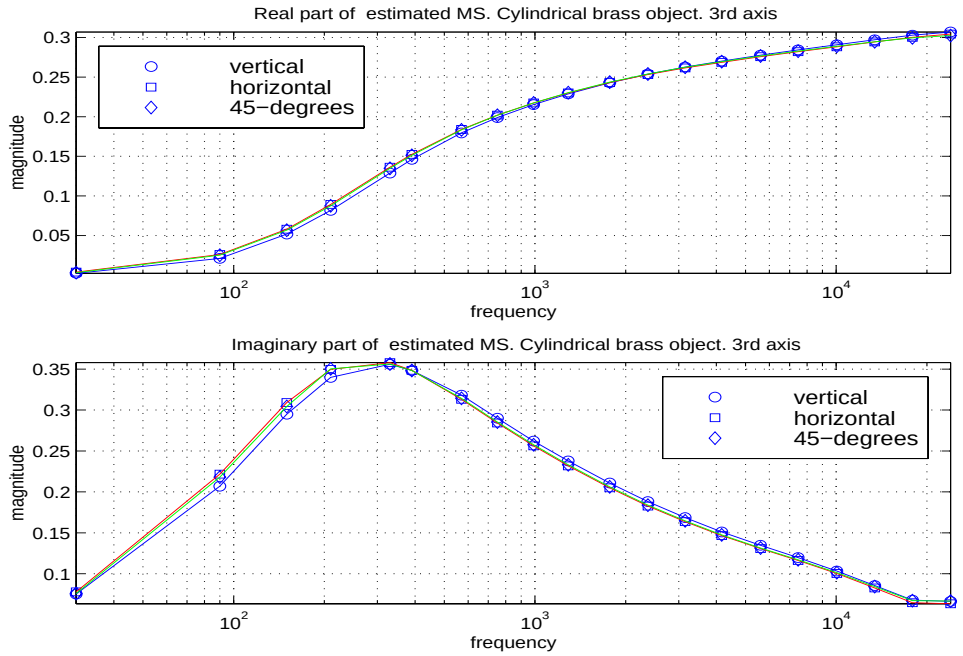

Figure 4.24: The real and imaginary part of estimated DMS of cylindrical brass object for the third axis according to Algorithm-I.

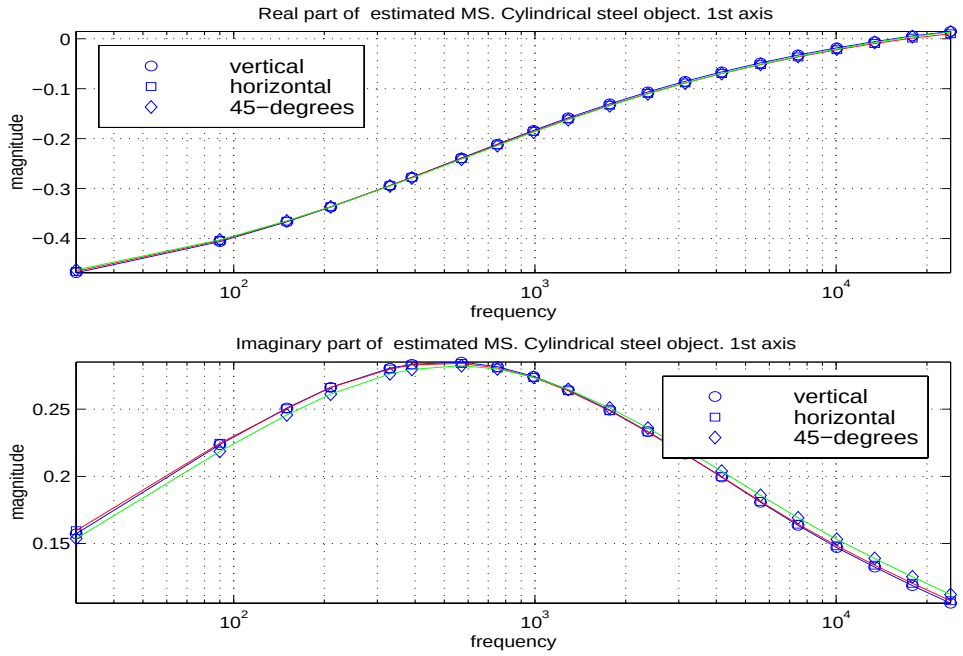

Figure 4.25: The real and imaginary part of estimated DMS of cylindrical steel object for the first axis according to Algorithm-I.

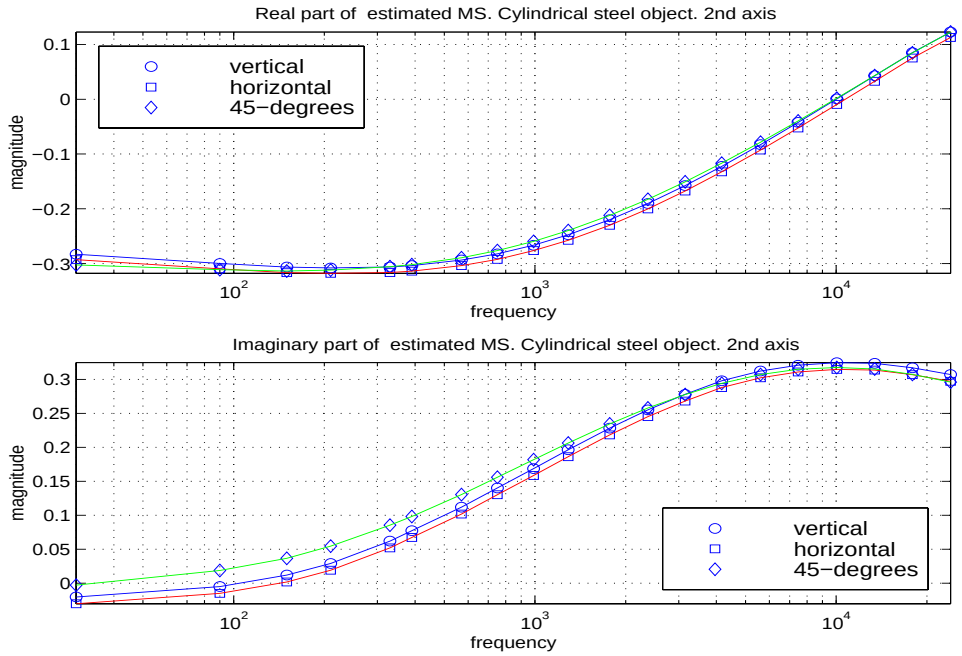

Figure 4.26: The real and imaginary part of estimated DMS of cylindrical steel object for the second axis according to Algorithm-I.

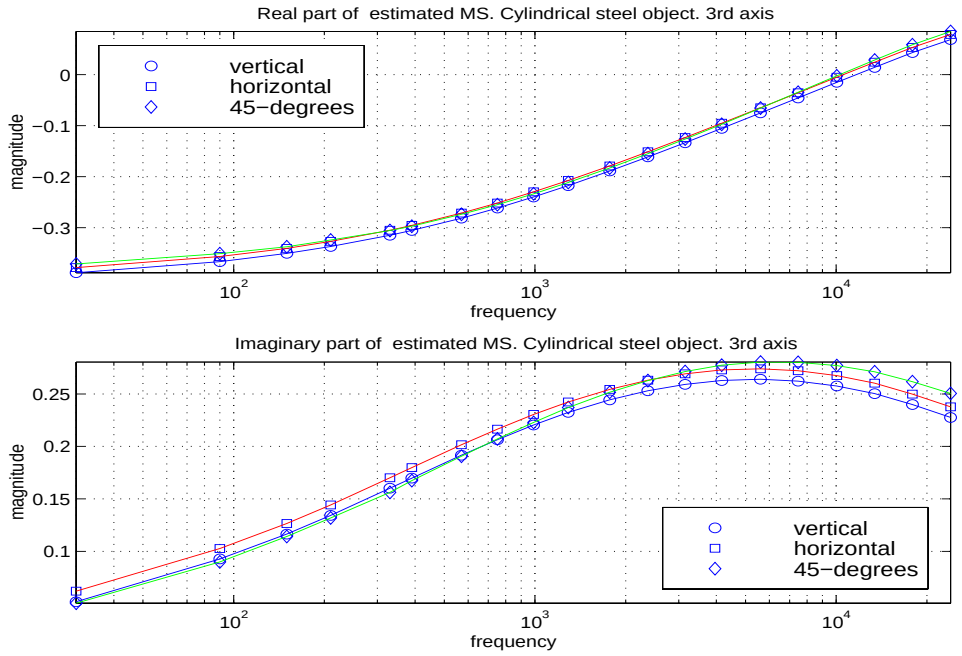

Figure 4.27: The real and imaginary part of estimated DMS of cylindrical steel object for the third axis according to Algorithm-I.

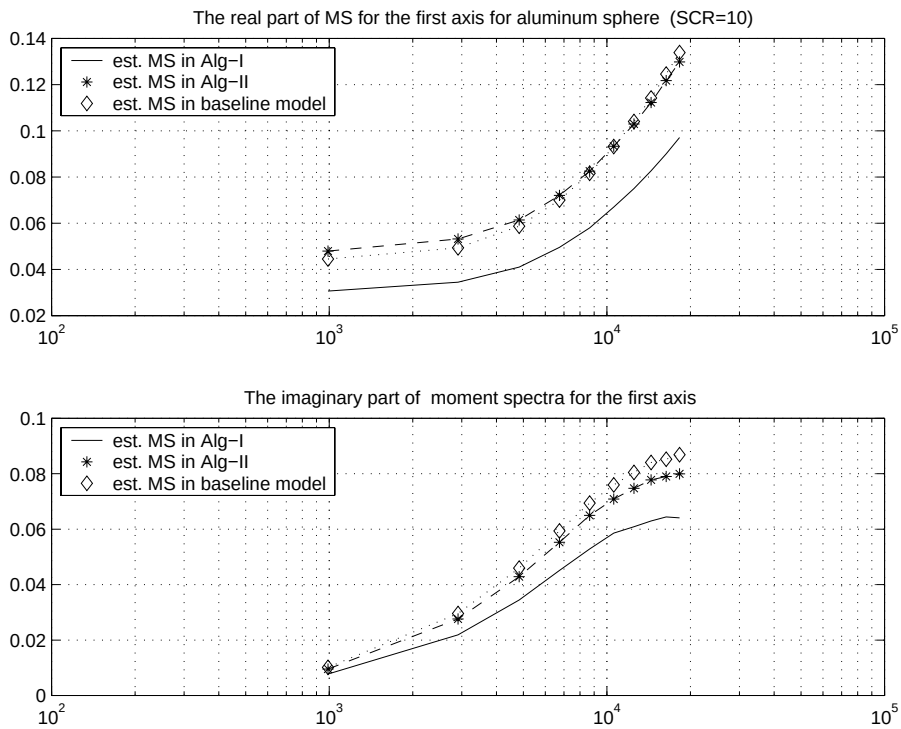

Figure 4.28: The real and imaginary part of estimated DMS of aluminum object according to Alg-I (after cleaning the data), and according to Alg-II and Baseline model (after adding noise to cleaned data) for the first axis.

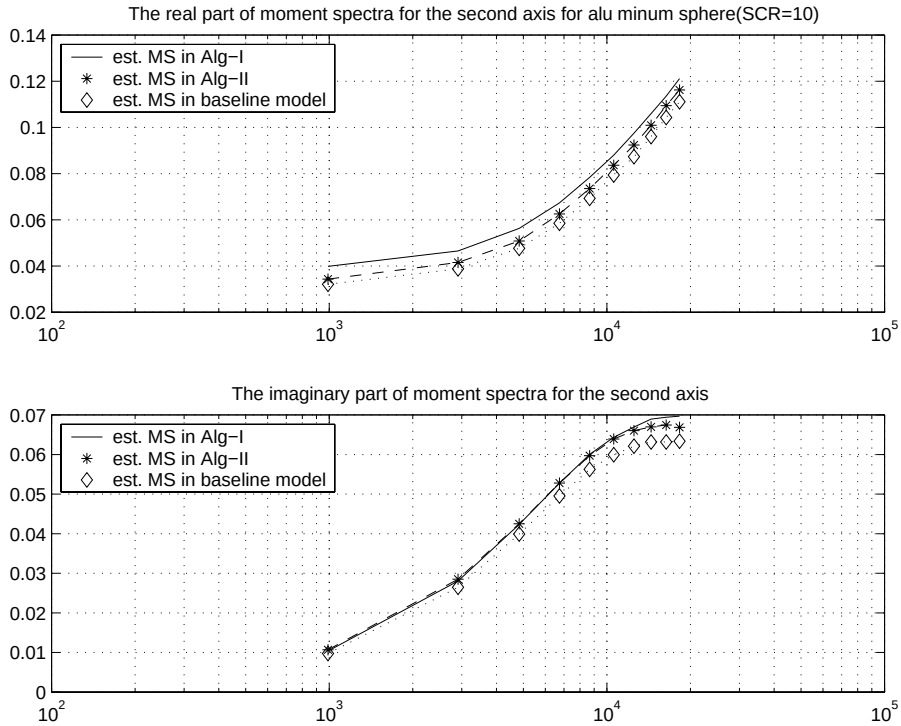

Figure 4.29: The real and imaginary part of estimated DMS of aluminum object according to Alg-I (after cleaning the data), and according to Alg-II and Baseline model (after adding noise to cleaned data) for the second axis.

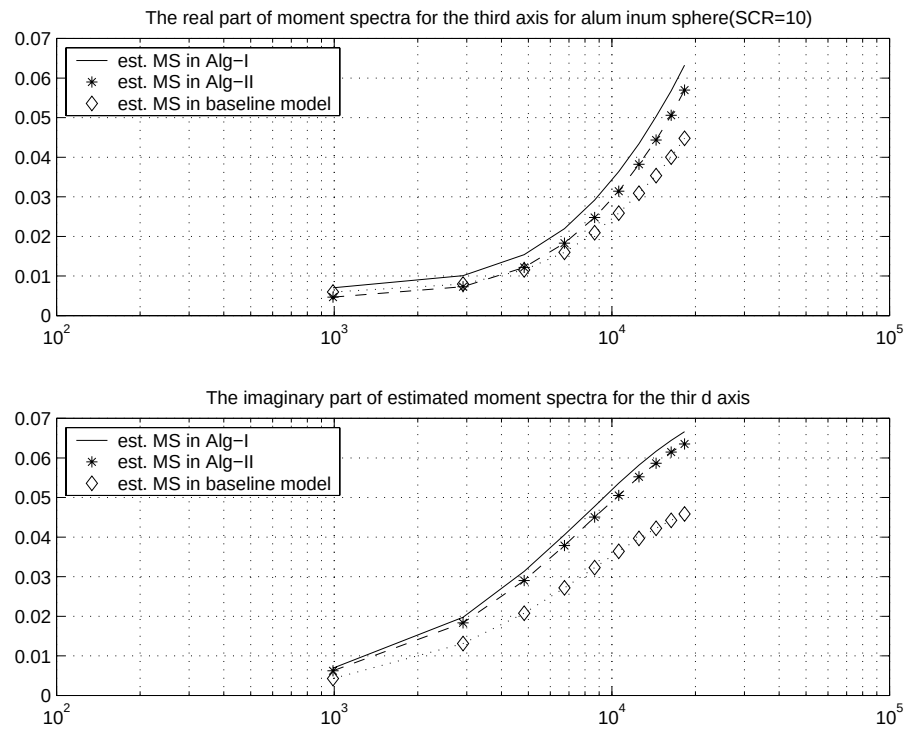

Figure 4.30: The real and imaginary part of estimated DMS of aluminum object according to Alg-I (after cleaning the data), and according to Alg-II and Baseline model (after adding noise to cleaned data) for the third axis.

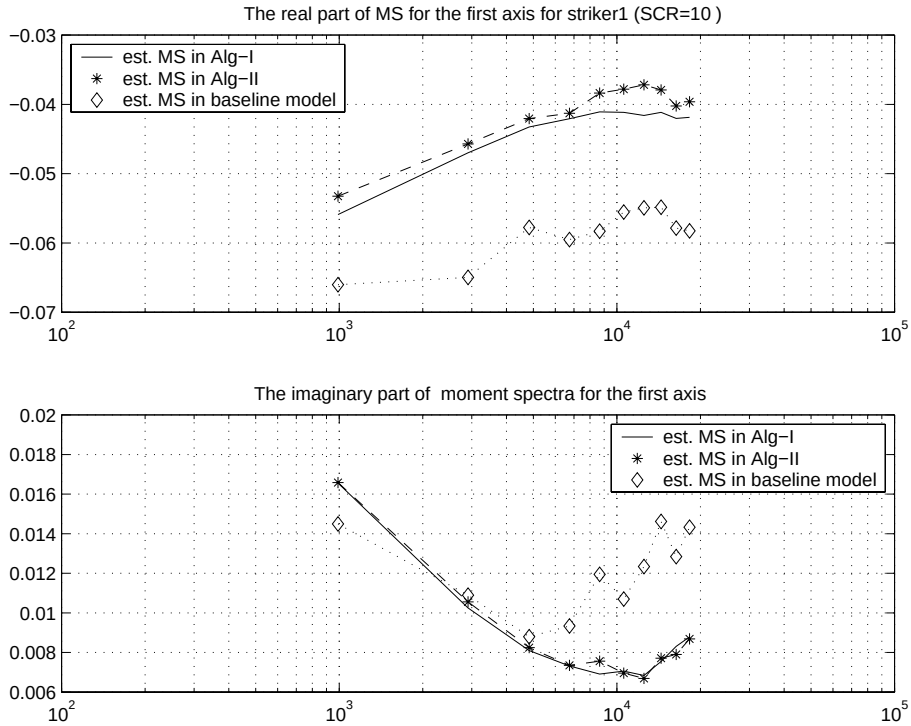

Figure 4.31: The real and imaginary part of estimated DMS of striker object according to Alg-I (after cleaning the data), and according to Alg-II and Baseline model (after adding noise to cleaned data) for the first axis.

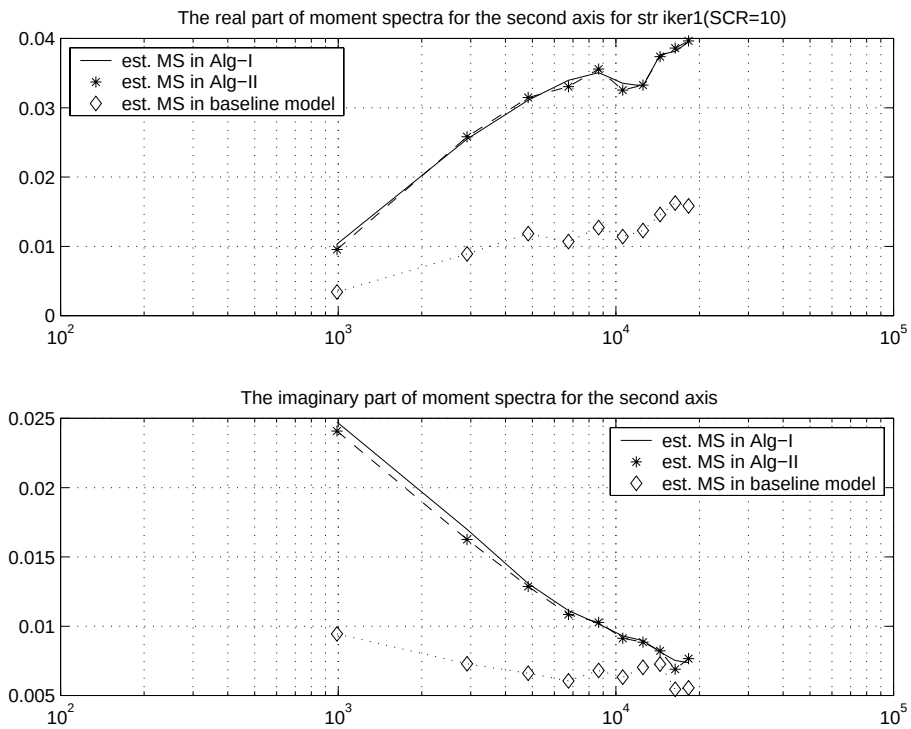

Figure 4.32: The real and imaginary part of estimated DMS of striker object according to Alg-I (after cleaning the data), and according to Alg-II and Baseline model (after adding noise to cleaned data) for the second axis.

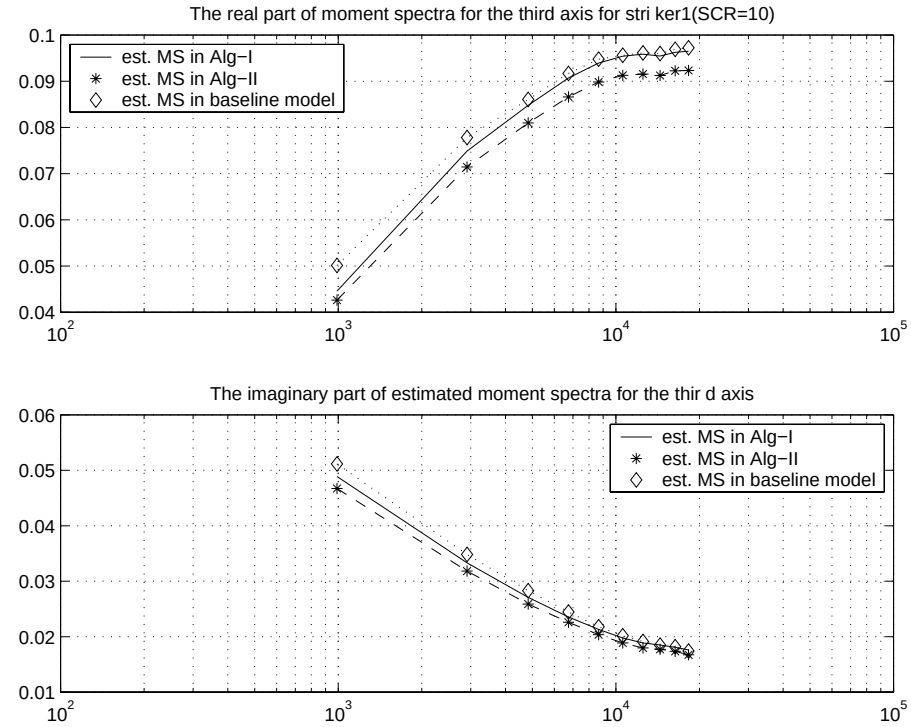

Figure 4.33: The real and imaginary part of estimated DMS of striker object according to Alg-I (after cleaning the data), and according to Alg-II and Baseline model (after adding noise to cleaned data) for the third axis.

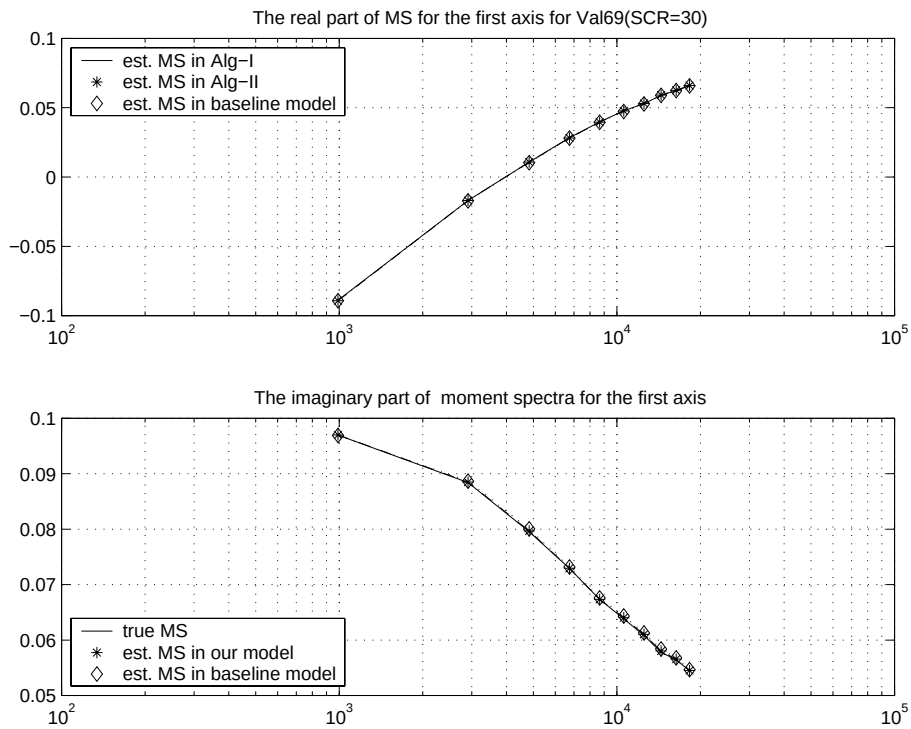

Figure 4.34: The real and imaginary part of estimated DMS of val69 object according to Alg-I (after cleaning the data), and according to Alg-II and Baseline model (after adding noise to cleaned data) for the first axis.

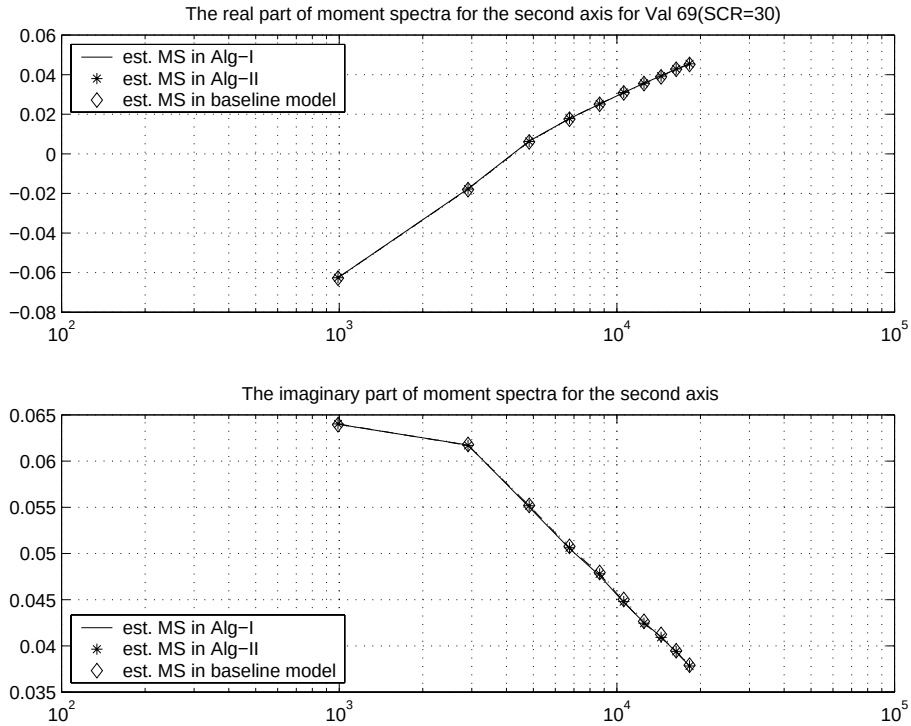

Figure 4.35: The real and imaginary part of estimated DMS of val69 object according to Alg-I (after cleaning the data), and according to Alg-II and Baseline model (after adding noise to cleaned data) for the second axis.

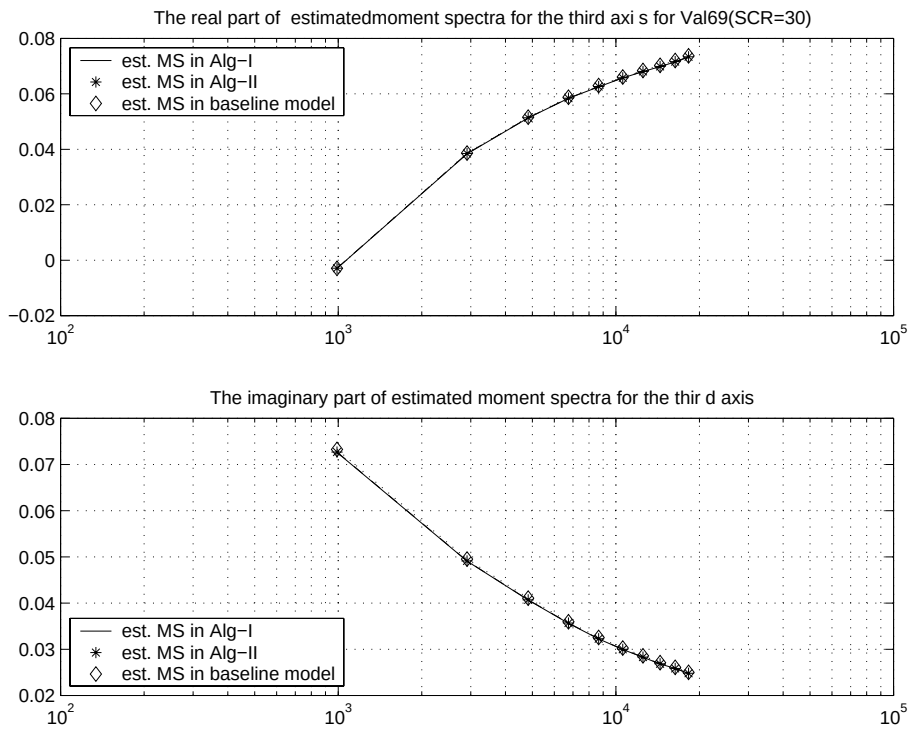

Figure 4.36: The real and imaginary part of estimated DMS of val69 object according to Alg-I (after cleaning the data), and according to Alg-II and Baseline model (after adding noise to cleaned data) for the third axis.

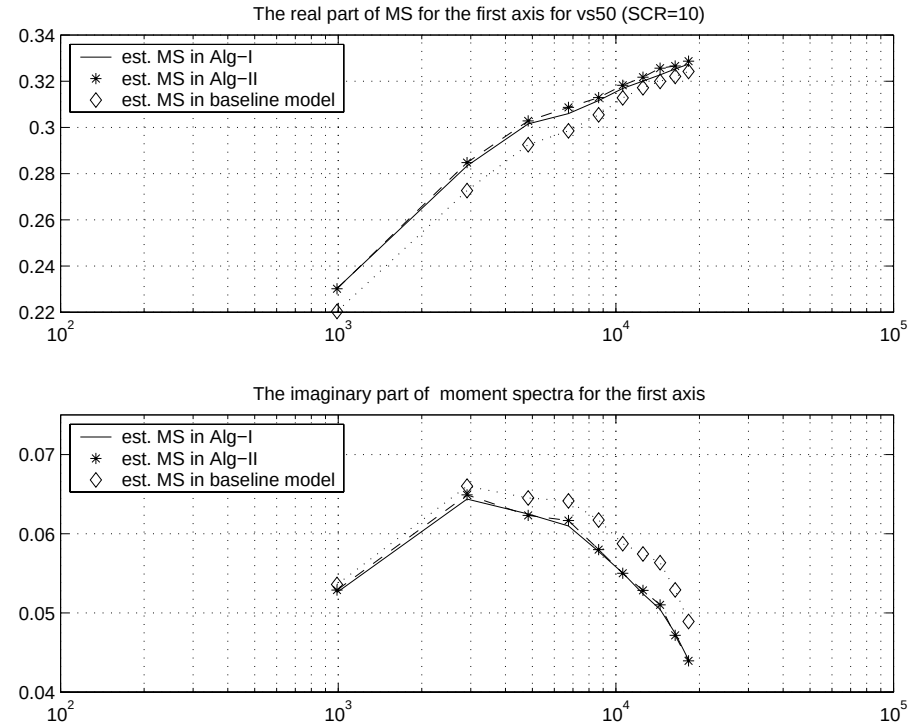

Figure 4.37: The real and imaginary part of estimated DMS of vs50 object according to Alg-I (after cleaning the data), and according to Alg-II and Baseline model (after adding noise to cleaned data) for the first axis.

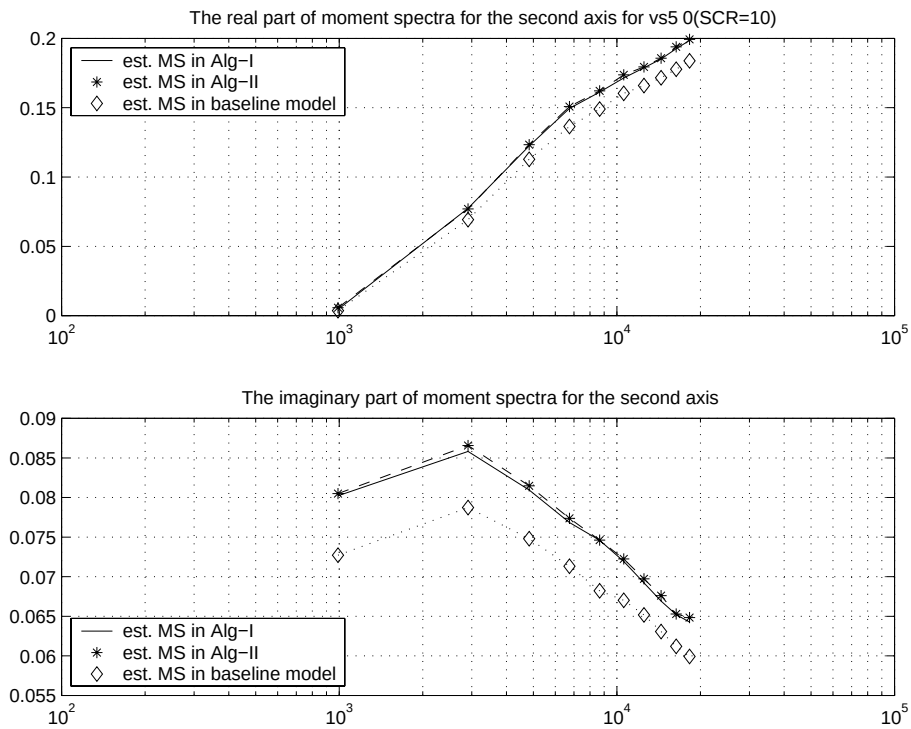

Figure 4.38: The real and imaginary part of estimated DMS of vs50 object according to Alg-I (after cleaning the data), and according to Alg-II and Baseline model (after adding noise to cleaned data) for the second axis.

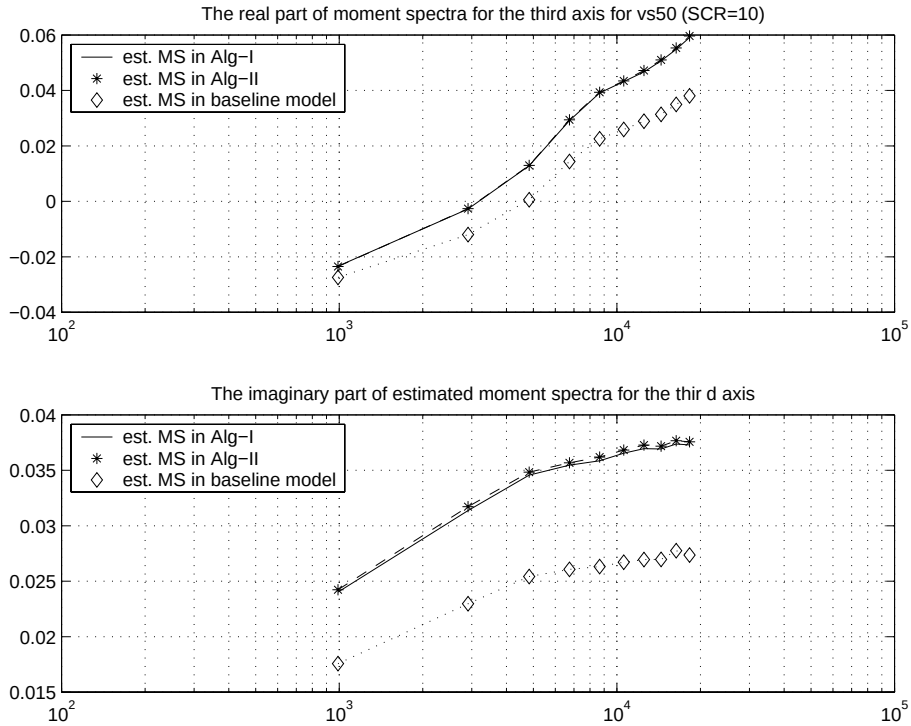

Figure 4.39: The real and imaginary part of estimated DMS of vs50 object according to Alg-I (after cleaning the data), and according to Alg-II and Baseline model (after adding noise to cleaned data) for the third axis.

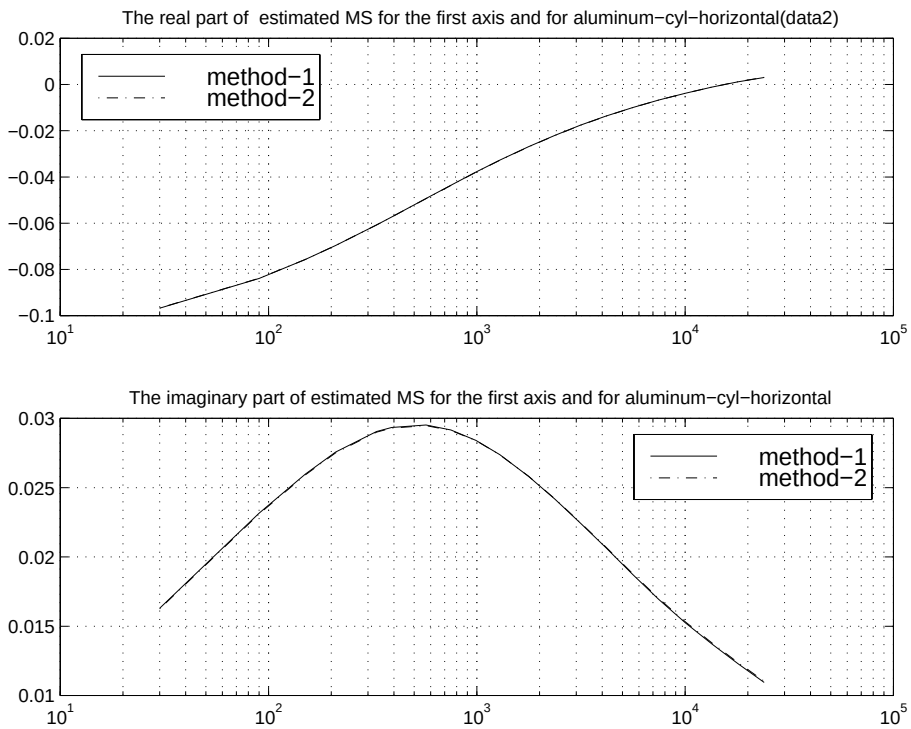

Figure 4.40: The real and imaginary part of estimated DMS of cylindarical steel object for the first axis according to both algorithms.

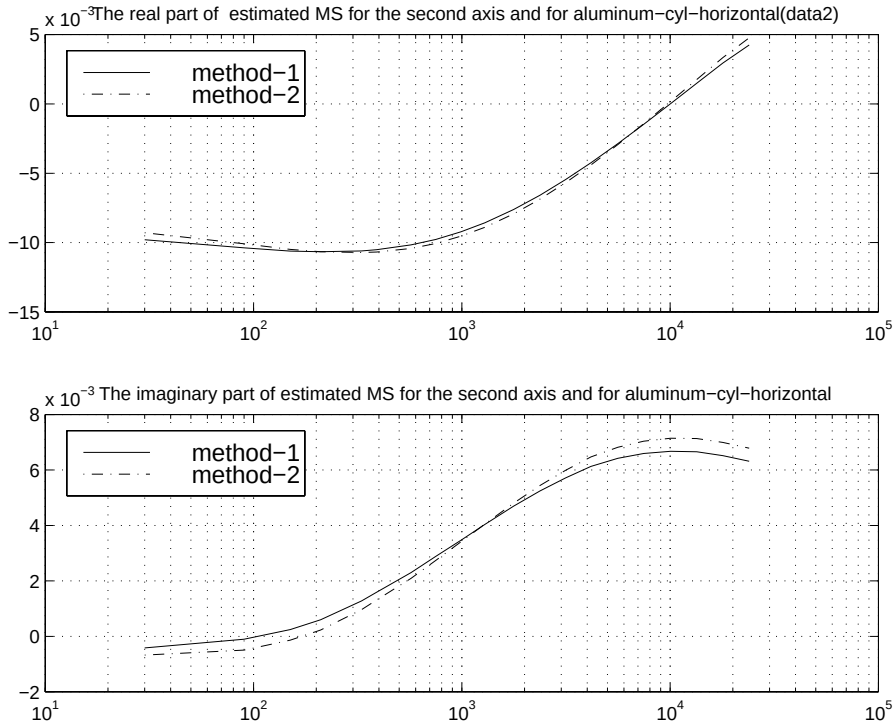

Figure 4.41: The real and imaginary part of estimated DMS of cylindarical steel object for the second axis according to both algorithms.

Chapter 5

Conclusion and Future Work

In this thesis, we have presented two approaches for the estimation of the DMS, the co-ordinates of the object center, and the rotation angles from BEMI data for the high metal content mines and for the estimation of same parameters after removing the estimation of clutter from the signal for the case of low metal content mines. Under these approach, the data are linearly related to the dipole moment spectra and non-linear functions of the object location and rotation angles. For the HMC mines, firstly, we determined the object center and rotation angles by using a low-dimensional non-linear optimization method. Then, we used the linear least square inversion procedure which determines the estimates of the DMS. For the LMC mines, we first estimated the distribution of clutter by using a stochastic model. Then, we determined the parameters of target after cleaning the signal.

While the results in this thesis are encouraging much work remains to be done in this area. First, the closed form analytical nature of the model makes it well suited to extensive performance analysis based on Cramer-Rao lower bounds on the variances of the estimated we obtain for anlges, location, and DMS. Using this performance metric allows one to start looking at issues of optimizing sensor configurations for particular detection/characterization problems. Moreover, in this work we assumed that we knew whether the targets of interest possessed spherical or ellipsoial symmetry. More interesting is the case where we estimate three rotation angles and three moment spectra and employ a statistical test to determine the symmetry characteristics of the underlying target. Again, performance analysis is also of interest. Finally, from a modeling perspective we are currently looking to techniques for mapping object charateristics (size, shape, and material paramaters) into the λ functions used in this model. As any such mapping represents an approximation to the true physics, it would be interesting to explore methods for doing this which explicitly minimize the error in the approximation.

Bibliography

[1] I. Won, D. Keiswetter, and E. Novikova, "Electromagnetic induction spectroscopy," *JEEG* **3**, pp. 27–40, March 1998.

[2] Y. Das, J. E. McFee, J. Toews, and G. C. Stuart, "Analysis of an electromagnetic induction detector for real-time localization of buried objects," *IEEE Trans. Geoscience and Remote Sensing* **28**, pp. 278–287, May 1990.

[3] M. Ozdemir, E. L. Miller, and S. Norton"Localization and characterization of buried objects from multi-frequency, array inductive data," in *SPIE'99 AeroSense Symposium,–Detection Technologies for Mines and Minelike Targets IV, Orlando Fl*, April 1998.

[4] M. Ozdemir, E. L. Miller, and A. Witten"Electromagnetic Modeling and Physics-based Processing Methods for Subsurface Object Characterization from Broadband Electromagnetic Induction Data ," in *Proceedings of the Progress in Electromagnetics Symposium, Boston MA*, July 2000.

[5] M. Ozdemir, E. L. Miller, and A. Witten"Clutter modelling and estimation methods for low metal content mine characterization from broadband electromagnetic induction data," in *Proceedings SPIE'00 AeroSense Symposium,–Detection Technologies for Mines and Minelike Targets V, Orlando Fl*, April 2000.

[6] P. C. Hansen, "The use of l-curve in the regularization of discrete ill-posed problems," *SIAM J. Sci. Comput.* **14**, pp. 1487–1503, 1993.

[7] P. C. Hansen, "Analysis of discrete ill-posed problems by means of the L-curve," *SIAM Review* **34**, pp. 561–580, December 1992.

[8] M. Belge, M. E. Kilmer, and E. L. Miller, "Simultaneous multiple regularization parameter selection by me ans of the l-hypersurface with applications to linear inverse problems posed in the wavelet domain," in *Proceedings of SPIE'98–Bayesian inference for inverse problems*, vol. 3459, July 1998.

[9] S. Hassani, "Foundations of Mathematical Physics," *Boston: Allyn and Bacon*, pp. 31–35, 1991.

[10] Barrow, B. and Khadr, N., "Performance of electromagnetic induction sensors for detecting and characterizing UXO," *UXO Forum*, Williamsburg VA, pp. 308-314.

[11] Barrow, B. and Nelson, H. H., "Model-based characterization of EM induction signatures for UXO/clutter discrimination using the MTADS platform," *UXO Forum*, Atlanta GA.

[12] Collins, L., Gao, P., and Carin, L., " An Improved Bayesian Decision Theoretic Approach for Land Mine Detection," *IEEE Transactionas on Geoscience and Remote Sensing*, vol. 37. no.2 pp. 811–819, Mar, 1999.

[13] Collins, L., Gao, P.,Geng, N., Carin, L., Keiswetter, D., and Won, I. J., " Discrimination of UXO-like metal targets using wideband electromagnetic induction," *UXO Forum '99*, Atlanta GA.

[14] Gao, P., Collins, L., Moulton, J., Makaowsky, L., Weaver, R., Keiswetter, D., and Won, I. J., " Enhanced Detection of Landmines using Broadband EMI Data, " *SPIE Conference on the Detection and Remediation of Mines and Minelike Targets III*, Orlando FL, pp. 1034–1043.

[15] N. Geng, C. E. Baum, and L. Carin, "On the low-frequency natural response of conducting and permeable targets," *IEEE Trans. Geoscience and Remote Sensing* **37**, pp. 347–359, January 1999.

[16] Keiswetter, D., Wonn, I. J., Bell, T., Barrow, B., and Khadr, N., " Electromagnetic Induction Spectroscopy," *UXO Forum '98*, Anaheim, CA.

[17] Khadr, N., Barrow, B. J., and Bell, T. H., " Target shape classification using electromagnetic induction sensor data," *UXO Forum '98*, Anheim CA.

[18] Miller, J., Keiswetter, D., Bell, T., Barrow, B., and Won, I. J., "Target Specific Information Content in Broadband EMI Data, "*SERDP Partners in Environmental Technology Symposium*, Washington, DC.

[19] Sower, G., Endsley, J., and Christy, E., "Discrimination of Metal Land Mines from Metal Clutter: Results of Field tests," *SPIE Conference on the Detection and Remediation of Mines and Minelike Targets IV*, Orlando, FL., pp. 78-88.

[20] Won, I. J., Keiswetter, D., and Novikova, E., "Electromagnetic Induction Spectroscopy," *JEEG*, vol. 3, pp.27-40, Mar, 1998.